ENSO Dynamics in the E3SM-1-0, CESM2, and GFDL-CM4 Climate Models

HAN-CHING CHEN,[a] FEI-FEI JIN,[a] SEN ZHAO,[a,b] ANDREW T. WITTENBERG,[c] AND SHAOCHENG XIE[d]

[a] *Department of Atmospheric Sciences, University of Hawai'i at Mānoa, Honolulu, Hawaii*
[b] *CIC-FEMD/ILCEC, Key Laboratory of Meteorological Disaster of Ministry of Education, and College of Atmospheric Science, Nanjing University of Information Science and Technology, Nanjing, China*
[c] *NOAA Geophysical Fluid Dynamics Laboratory, Princeton, New Jersey*
[d] *Lawrence Livermore National Laboratory, Livermore, California*

(Manuscript received 4 May 2021, in final form 23 July 2021)

ABSTRACT: This study examines historical simulations of ENSO in the E3SM-1-0, CESM2, and GFDL-CM4 climate models, provided by three leading U.S. modeling centers as part of the Coupled Model Intercomparison Project phase 6 (CMIP6). These new models have made substantial progress in simulating ENSO's key features, including amplitude, time scale, spatial patterns, phase-locking, the spring persistence barrier, and recharge oscillator dynamics. However, some important features of ENSO are still a challenge to simulate. In the central and eastern equatorial Pacific, the models' weaker-than-observed subsurface zonal current anomalies and zonal temperature gradient anomalies serve to weaken the nonlinear zonal advection of subsurface temperatures, leading to insufficient warm/cold asymmetry of ENSO's sea surface temperature anomalies (SSTA). In the western equatorial Pacific, the models' excessive simulated zonal SST gradients amplify their zonal temperature advection, causing their SSTA to extend farther west than observed. The models underestimate both ENSO's positive dynamic feedbacks (due to insufficient zonal wind stress responses to SSTA) and its thermodynamic damping (due to insufficient convective cloud shading of eastern Pacific SSTA during warm events); compensation between these biases leads to realistic linear growth rates for ENSO, but for somewhat unrealistic reasons. The models also exhibit stronger-than-observed feedbacks onto eastern equatorial Pacific SSTAs from thermocline depth anomalies, which accelerates the transitions between events and shortens the simulated ENSO period relative to observations. Implications for diagnosing and simulating ENSO in climate models are discussed.

KEYWORDS: Dynamics; ENSO; Climate models; Atmosphere-ocean interaction

1. Introduction

El Niño–Southern Oscillation (ENSO) is the most prominent phenomenon of year-to-year fluctuation of the global climate system. It is characterized by large-scale warm (cold) sea surface temperature anomalies (SSTA) in the central/eastern equatorial Pacific Ocean, known as El Niño (La Niña) events, which occur irregularly every 2–7 years. The ENSO events generally onset in boreal spring, growing during the summer and fall, and usually peak in boreal wintertime, called the phase-locking phenomenon. ENSO's basin-scale surface temperature fluctuations are accompanied by changes in atmospheric and oceanic circulations that affect not only the global climate system, but also marine and terrestrial ecosystems, fisheries, and human activities. The primary dynamical mechanisms for the ENSO phenomenon have been extensively studied over the past decades. ENSO is understood as a leading coupled ocean–atmospheric mode of the tropical Pacific essentially described by the simple conceptual delayed oscillator or recharge oscillator (RO) paradigm (e.g., Cane and Zebiak 1985; Suarez and Schopf 1988; Battisti and Hirst 1989; Philander 1990; Jin and Neelin 1993; Neelin et al. 1994; Jin 1997a,b; Neelin et al. 1998; Wang and Picaut 2004).

The state-of-the-art climate models almost all faithfully simulate basic features of ENSO in terms of overall spatial pattern and interannual periodicity. However, the ability to simulate ENSO complexity varies enormously among the current generation of climate models (Guilyardi et al. 2009; Guilyardi et al. 2012; Bellenger et al. 2014; Capotondi et al. 2015; Chen et al. 2017; Capotondi et al. 2020a,b; Guilyardi et al. 2020). In fact, a detailed analysis of coupled dynamics revealed significant biases in simulating ENSO feedback processes. For instance, Guilyardi et al. (2009) and Lloyd et al. (2009) noted that the dynamic feedback efficiency or the atmospheric Bjerknes positive feedback parameter—a measure of the strength of the ENSO zonal wind anomalies response per degree of SSTA—is systematically weak for a significant number of climate models. They also noted that the thermodynamic feedback, measured by the net anomalous surface heat flux response per degree of SSTA, is also systematically weak. A linear analysis of the recharge oscillator framework provides a simple and powerful way to understand and evaluate the ENSO growth rate [the Bjerknes index of Jin et al. (2006)] in both reanalysis data and coupled model simulations. The dynamic feedback positively contributes to the ENSO growth rate as measured by the Bjerknes index (BJ index), while the thermodynamic feedback usually contributes to the BJ index negatively. These systematic and opposite errors in dynamic and thermodynamic feedbacks tend to compensate each other

Supplemental information related to this paper is available at the Journals Online website: https://doi.org/10.1175/JCLI-D-21-0355.s1.

Corresponding author: Fei-Fei Jin, jff@hawaii.edu

DOI: 10.1175/JCLI-D-21-0355.1

in the total BJ index. Kim and Jin (2011) conducted a detailed analysis of the BJ index in the IPCC AR4 models and showed that most models underestimate the dynamic and thermodynamic feedbacks. More recently, Bayr et al. (2018, 2019) demonstrated that ENSO's positive dynamic feedback and negative thermodynamic feedback are strongly linearly related through biases in the mean state. They showed clearly that biases in these two feedbacks partly compensate each other in many climate models. Significant biases in climate mean state, errors in the physical processes, and inadequacies in capturing across-scale interactions are clearly the key sources that hinder the climate model's faithful simulation of ENSO and its complexity.

Asymmetry in SSTA between El Niño and La Niña events is an intrinsic nonlinear characteristic of ENSO and often measured by the skewness of SST variability. The observed SSTA has highly positive skewness in the eastern Pacific where the ENSO-related SST variability is strongest. However, most climate models fail to reproduce ENSO asymmetry, either underestimating the positive asymmetry found in the observations or having negative asymmetry (Bellenger et al. 2014; An et al. 2005; Zhang and Sun 2014). The possible reason for the weak ENSO asymmetry in simulations may be due to the weak nonlinear air–sea interaction, which is associated with the cold biases in the equatorial central Pacific that confine the westerly wind anomaly to the western Pacific (Sun et al. 2016). Recently, Hayashi et al. (2020) demonstrated that simulated asymmetry of ENSO is highly correlated with subsurface nonlinear dynamical heating (NDH) along the equatorial thermocline.

Another notable bias in the representation of ENSO in climate models is that the center of the ENSO-related SSTA over the tropical Pacific shifts to the west (Kug et al. 2012) and extends too far into the western Pacific, where there is a negative (positive) SSTA in the observations during El Niño (La Niña). The excessive westward extension of the SSTA associated with ENSO could affect the ability of models to simulate realistic teleconnections (Leloup et al. 2008; Yu and Kim 2010; Bellenger et al. 2014). Some studies argue that this bias appears to arise from the intensity of the eastern Pacific cold tongue, which suppresses the local convection over the eastern Pacific due to the decrease of total SST, resulting in an atmospheric deep convection confined to the central-western Pacific (Ham and Kug 2012, 2015). Graham et al. (2017) also found that, in climate models, the westward extension of the cold tongue along with overly strong westward mean zonal currents near the edge of the western Pacific warm pool will produce unrealistic western warm anomalies due to the zonal advection process.

Although most climate models appear to successfully simulate ENSO, there is strong evidence that these models often achieve realistic levels of ENSO activity for the wrong reasons (Vijayeta and Dommenget 2018). Climate models remain deficient in simulating the observed ENSO spatial and temporal complexity that involves interplays of coupled dynamic and thermodynamic feedbacks, interactions across multiple scales, nonlinear processes in the tropical atmosphere and ocean systems, biases in mean state and physical processes, and influences external to the equatorial Pacific coupled ENSO dynamics (Timmermann et al. 2018). Although the CLIVAR 2020 ENSO metric package is available for model diagnosis, comparison, and evaluation (Planton et al. 2021), it provides only a basic view of ENSO features. To ensure reliable sensitivities, predictions, and projections of ENSO, it is important to capture the correct underlying ENSO feedbacks, not just the salient features. In this study, we aim to advance predictive and process-level understandings of ENSO simulated in the Energy Exascale Earth System Model version 1 (E3SM-1-0), the Community Earth System Model version 2 (CESM2), and the Geophysical Fluid Dynamics Laboratory's CM4.0 (GFDL-CM4). These models are provided by three leading U.S. modeling centers as part of the CMIP6 with significant updates on their atmospheric and ocean components and have a better overall performance of ENSO features, including spatial patterns, amplitude, and frequency. To better understand the broad range of interactive processes and sources that control the fundamental properties of ENSO in climate models and observations, we use a hierarchy of coupled dynamical frameworks consisting of theoretical analysis and coupled dynamic diagnostics.

This paper is arranged as follows. Section 2 introduces the climate models, observational datasets, and the methodology used in this study. In section 3, the fundamental characteristics of ENSO are examined, including spatial patterns, temporal structures, fundamental recharge oscillator dynamics, and atmospheric responses. The detailed ENSO dynamics and feedbacks are discussed in section 4 by analyzing the heat budget, Bjerknes stability, Wyrtki periodicity, and subsurface nonlinear dynamical heating. Section 5 gives conclusions and discussion.

2. Data and methods

a. *Model descriptions and observations*

In this study, the E3SM-1-0, CESM2, and GFDL-CM4 climate models are analyzed, and the descriptions of these models are provided in Table 1.

E3SM-1-0 is a new fully coupled state-of-the-science Earth system model from the U.S. Department of Energy (DOE), which started with CESM1 as E3SM v0. It consists of five interacting components: global atmosphere, land surface, ocean, sea ice, and rivers. The E3SM Atmosphere Model (EAM) is based on the Community Atmosphere Model version 5.3 (CAM5.3) with a spectral-element dynamical core, increased vertical levels from 30 to 72, and notable improvements in model physics (Rasch et al. 2019; Xie et al. 2018). The land component is based on the Community Land Model version 4.5 (CLM4.5) with new soil hydrology, carbon–nitrogen–phosphorus (CNP) cycle, and other new biogeochemistry representations. E3SM-1-0 includes new ocean, sea ice, and land ice models based on the Model for Prediction Across Scales (MPAS), which uses spherical centroidal Voronoi tessellations (SCVTs) for multiresolution modeling to replace the ocean and ice components in CESM1. More details on all the component models can be found in Golaz et al. (2019).

CESM2 is the most recent version of the Earth system model developed by the National Center for Atmospheric Research

TABLE 1. List of models and their ocean and atmosphere components, resolutions, used ensemble members, and key references.

	E3SM-1-0	CESM2	GFDL-CM4
Atmospheric model	EAM	CAM6	GFDL-AM4.0.1
	90 × 90 × 6 lon/lat/cube faces	288 × 192 lon/lat	360 × 180 lon/lat
	72 levels	32 levels	33 levels
	Top level 0.1 hPa	Top level 2.25 hPa	Top level 1 hPa
Ocean model	MPAS-Ocean	POP2	GFDL-OM4p25
	60 to 30 km	320 × 384 lon/lat	1440 × 1080 lon/lat
	60 levels	60 levels	75 levels
	Top grid cell 0–10 m	Top grid cell 0–10 m	Top grid cell 0–2 m
Ensemble members	r1i1p1f1, r2i1p1f1, r3i1p1f1, r4i1p1f1	r1i1p1f1, r2i1p1f1, r3i1p1f1, r4i1p1f1	r1i1p1f1
References	Golaz et al. (2019) and Caldwell et al. (2019)	Danabasoglu et al. (2020)	Held et al. (2019)

(NCAR). It includes fully coupled ocean, atmosphere, land, ice, rivers, and marine biogeochemistry components with many improvements since its previous version, CESM1. The atmospheric component, the Community Atmospheric Model version 6 (CAM6), uses the same finite volume (FV) dynamical core as in CESM1 with many improved representations of physical processes. The ocean component is based on Parallel Ocean Program version 2 (POP2), which is the same as in CESM1 but includes several physical and numerical improvements. A detailed description of CESM2 is provided in Danabasoglu et al. (2020).

GFDL-CM4, one of GFDL's latest multipurpose atmosphere–ocean coupled climate models, is built with the AM4.0 atmosphere model, LM4.0 land model, and OM4.0 ocean model. The AM4.0 atmosphere model's dynamical core is the cubed-sphere finite volume (FV3) hydrostatic version modified from AM3. The ocean component OM4.0 is based on MOM6 at 1/4° resolution with 75 levels using hybrid pressure/isopycnal vertical coordinate. The land component of CM4.0 has dynamic vegetation similar to that used in LM3. The SIS2 sea ice model used in CM4.0 is a significant improvement over the SIS model in previous generations of GFDL models. More details about GFDL-CM4 can be found in Held et al. (2019)

E3SM-1-0, CESM2, and GFDL-CM4 have all contributed simulations to phase 6 of the Coupled Model Intercomparison Project (CMIP6; Eyring et al. 2016), including preindustrial, historical, and future scenario simulations. For this study, we will focus on the historical simulations and use four ensemble members for E3SM-1-0 and CESM2 (r1i1p1f1, r2i1p1f1, r3i1p1f1, r4i1p1f1) and one ensemble member for GFDL-CM4 (r1i1p1f1). Each historical simulation is conducted from a preindustrial control simulation and then forced by the historical forcing data provided by CMIP6 from 1850 to 2014.

In this study, observed ocean temperature, ocean current, and thermocline depth are obtained from four reanalysis products: the Ocean Reanalysis System 5 (ORAS5) for 1958–2018 (Zuo et al. 2019), the Simple Ocean Data Assimilation reanalysis version 3.3.1 (SODA331) for 1980–2015 (Carton et al. 2018), the Simple Ocean Data Assimilation reanalysis version 2.2.4 (SODA224) for 1950–2010 (Giese and Ray 2011), and the National Centers for Environmental Prediction Global Ocean Data Assimilation System (GODAS) for 1980–2019 (Behringer and Xue 2004). The SST was derived from the nearest-surface temperature of each reanalysis dataset. The wind stress and net surface heat flux are from ORAS5. The specific humidity, surface shortwave radiation, surface longwave radiation, surface latent heat flux, and surface sensible heat flux are from the fifth generation of ECMWF atmospheric reanalysis of the global climate (ERA5; Hersbach et al. 2020) for 1958–2018. The precipitation is from Global Precipitation Climatology Project (GPCP; Adler et al. 2003) monthly precipitation analysis (1979–2018). The anomalies here are based on the climatology from 1850 to 2014 for models' output and each reanalysis dataset period for observations. The linear trend is removed from data using a least squares best-fit line. Although these reanalysis products have inherent uncertainties, which may come from model parameterizations, observational uncertainties, and the data assimilation methods, the results are consistent for each reanalysis dataset in this study.

b. Recharge oscillator framework

By reducing the linear ENSO dynamics into two prognostic equations for the eastern equatorial Pacific SSTA (T_E) and western equatorial Pacific thermocline depth anomalies (h_w), the linear ENSO dynamics based on recharge oscillator framework (Jin 1997a) can be written as

$$\frac{dT_E}{dt} = RT_E + F_1 h_w, \tag{1}$$

$$\frac{dh_w}{dt} = -rh_w - F_2 T_E, \tag{2}$$

where R and F_1 are the SST growth rate and phase-transition rate, and r and F_2 are the thermocline damping rate and phase-transition rate. In this study, T_E and h_w are the area-averaged eastern equatorial Pacific SSTA (Niño-3 index; 5°S–5°N, 150°–90°W) and western equatorial Pacific thermocline anomalies (5°S–5°N, 120°E–155°W), respectively. Since there are significant SST anomalies over the Niño-3 region in the first empirical orthogonal function (EOF) of SSTA in observations and most CMIP models, we here select the Niño-3 index to investigate the leading-order ENSO dynamics.

To assess the stability and periodicity of ENSO, we use the Bjerknes–Wyrtki–Jin (BWJ) indices defined by Jin et al. (2020), with modifications from S. Zhao and F.-F. Jin (2021, unpublished manuscript). Applying the linear relationships arising

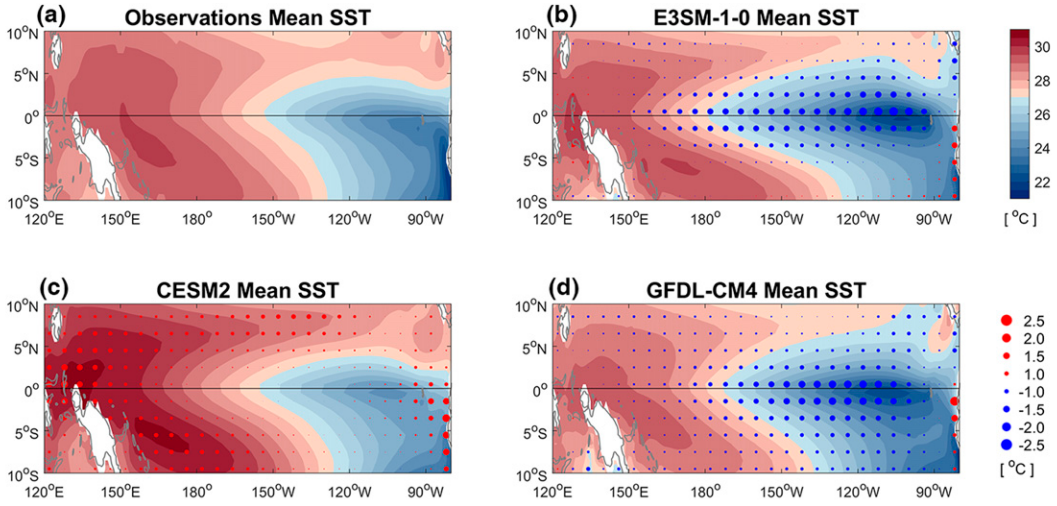

FIG. 1. (a) Observations, (b) E3SM-1-0, (c) CESM2, and (d) GFDL-CM4 mean SST (shading) and bias of mean SST (dots). The mean SST bias is calculated by subtracting the observed SST climatology from simulated SST climatology.

from a quasi-balance approximation, the Bjerknes stability (I_{BJ}) and Wyrtki frequency (I_{WJ}) indices can be expressed as

$$I_{BJ} = \frac{R - r}{2}, \tag{3}$$

and

$$I_{WJ} = \frac{4\pi}{\sqrt{4F_1F_2 - (R + r)^2}}. \tag{4}$$

The numerator of (3) can be partitioned into a thermodynamic component R_{TD} and a dynamic component $R_{DYN} = (R - r) - R_{TD}$. The advantage of using BWJ indices comes from their decomposition of the contributions to the ENSO growth rate and periodicity from different coupled processes. Further details are provided in the appendix. We verified that there is no significant difference in ENSO characteristics between model ensemble members, and so only the first ensemble member (r1i1p1f1) from each model is used in the following BJ and WJ analyses.

c. Mixed layer heat budget analysis

To investigate the contribution of different oceanic processes to SSTA, we analyze the ocean mixed layer heat budget here. The mixed layer temperature anomaly tendency equation is expressed as

$$\frac{\partial \langle T' \rangle}{\partial t} = \underbrace{-\left\langle \overline{u}\frac{\partial T'}{\partial x}\right\rangle - \left\langle u'\frac{\partial \overline{T}}{\partial x}\right\rangle - \left\langle u'\frac{\partial T'}{\partial x}\right\rangle}_{\text{zonal advection}}$$
$$\underbrace{-\left\langle \overline{v}\frac{\partial T'}{\partial y}\right\rangle - \left\langle v'\frac{\partial \overline{T}}{\partial y}\right\rangle - \left\langle v'\frac{\partial T'}{\partial y}\right\rangle}_{\text{meridional advection}}$$
$$\underbrace{-\left\langle \overline{w}\frac{\partial T'}{\partial z}\right\rangle - \left\langle w'\frac{\partial \overline{T}}{\partial z}\right\rangle - \left\langle w'\frac{\partial T'}{\partial z}\right\rangle}_{\text{vertical advection}} + \frac{Q'}{\rho_0 C_p H}$$
$$+ \text{Residual}, \tag{5}$$

where the angle brackets represent the depth average within the mixed layer; T is the ocean temperature; u, v, and w are the zonal, meridional, and vertical ocean currents; Q, ρ_0, C_p, and H are the surface heat flux, seawater density, specific heat of seawater, and mixed layer depth (set to 50 m here). The primes and overbars indicate the anomaly and seasonal climatology of variables, respectively.

3. Fundamental characteristics of ENSO

a. Spatial pattern of SST variability

The ENSO characteristics (such as amplitude, time scale, and spatial pattern) are largely dependent on the Pacific mean state. In particular, the mean SST and mean zonal SST gradient are key parameters for determining ENSO's growth rate and frequency. The observed SST climatology is shown in Fig. 1 for comparison with E3SM-1-0, CESM2, and GFDL-CM4. The equatorial cold tongue in E3SM-1-0 and GFDL-CM4 extends too far westward, and there is a significant cold bias in the central-eastern Pacific from the enhancement of the eastern Pacific cold tongue (Figs. 1b,d). In contrast, in CESM2, the warm biases appear in the far eastern and western Pacific, while there is only a very weak cold bias in the central Pacific (Fig. 1c).

We next focus on the spatial distributions of SST variability by showing the standard deviation of monthly SSTA in Figs. 2a–d. The observations exhibit the largest standard deviation in the eastern Pacific and off the coast of Peru. In E3SM-1-0 and CESM2 the amplitude of SSTA is overestimated in the central/eastern tropical Pacific relative to observations, while GFDL-CM4 is closer to the observed values. In addition to the amplitude, the spatial pattern of the SST variability also shows differences with the observed. In E3SM-1-0 and GFDL-CM4, the significant standard deviations (standard deviations larger than 1°C) are achieved about 160° and 170°W, respectively, which are similar to the observed variability (~170°W); however, in CESM2 it extends too far westward

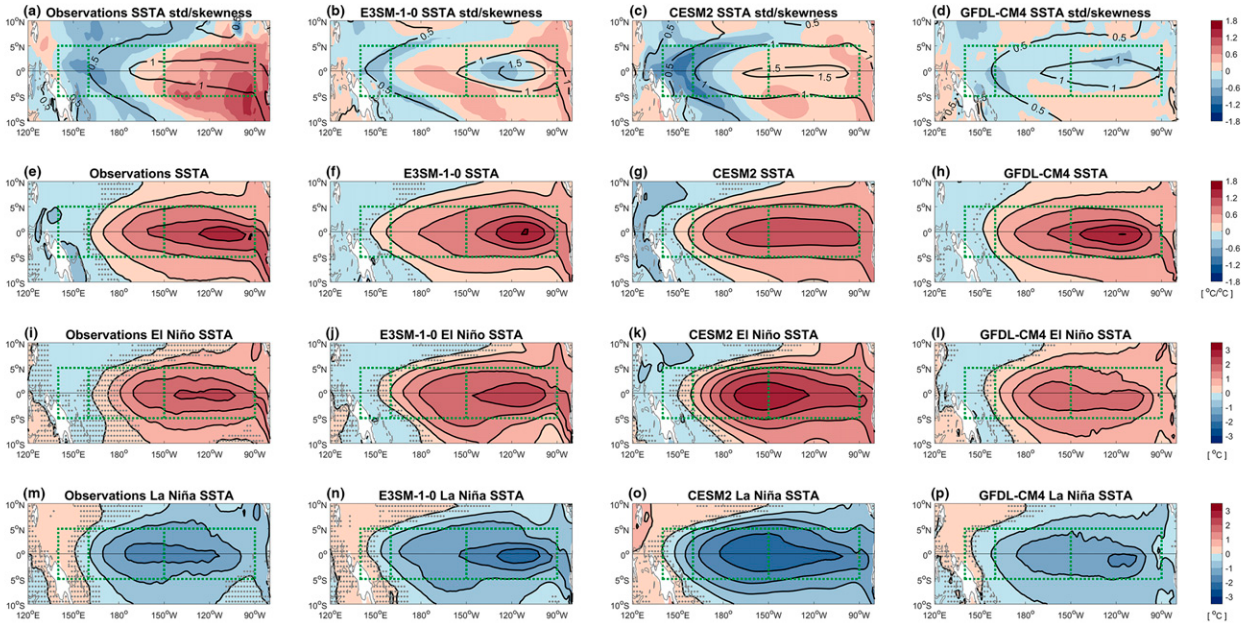

FIG. 2. The spatial pattern of SST variability in observations, E3SM-1-0, CESM2, and GFDL-CM4 for (a)–(d) standard deviation (contours) and skewness (shading) of monthly SSTA, (e)–(h) regression of SSTA onto the Niño-3 index, (i)–(l) composite of DJF SSTA for winter peaks El Niño, and (m)–(p) composite of DJF SSTA for winter peaks La Niña. The three rectangles from west to east represent the region for equatorial western Pacific, Niño-4, and Niño-3, respectively. Gray dots indicate the shading values that are not statistically significant at the 95% confidence level.

(near 160°E). Moreover, the area of large variability is confined close to the equator around 2°S–2°N in observations, but E3SM-1-0 and CESM2 show a wider meridional extension. We looked at spatial distributions of SST variability and selected the Niño-3 region (5°S–5°N, 150°–90°W), which has a significant standard deviation both in observations and models, to calculate the index used to define El Niño and La Niña events. The spatial patterns of SST associated with Niño-3 index are obtained by regressing SSTA at each grid point onto the Niño-3 index (Figs. 2e–h), and are consistent with the standard deviation distribution.

To evaluate the spatial pattern of the SSTA in El Niño and La Niña events, the composite of DJF SSTA for winter peaks El Niño (La Niña) events greater than 1.0 standard deviation (less than −1.0 standard deviations) is shown in Figs. 2i–l (Figs. 2m–p). The observed El Niño SSTA has a similar pattern to the regression map, which exists where the SSTA is largest in the Niño-3 region, while the location of maximum La Niña SSTA shifts to west in the central Pacific with a smaller amplitude of SSTA compared to that of El Niño. However, in the climate models, the asymmetry in the spatial distribution and amplitude of SSTA between El Niño and La Niña is much smaller. As noted in the composite analysis, there is an apparent asymmetric amplitude of SSTA between El Niño and La Niña that can be expressed by the skewness, as shown by the shading in Figs. 2a–d. In the eastern Pacific where the SST variability is strongest, the observed SSTA has a value of positive skewness, indicating that the observed SSTA are skewed toward warm events in the eastern Pacific; however, all three models underestimated the positive asymmetry, especially in GFDL-CM4, which shows negative SSTA skewness. The details of poor simulation of ENSO skewness will be discussed in section 4c.

Another notable bias of ENSO-related SST variability is found in climate models, where the edge of SSTA in model simulations extends more westward than the observed result. There is a negative SSTA in the observations during El Niño in the western Pacific, while the positive SSTA extends too far into the far western Pacific in all three models (Figs. 2e–h). The excessive westward extension of the SSTA is significant for both El Niño and La Niña events, and the edge of SSTA in La Niña events extends more westward than El Niño due to the nonlinear effect of atmospheric response (Figs. 2i–p). The causes for the SSTA edge extension bias will be discussed later (section 4a).

b. *Time series structure of ENSO*

To better understand the statistical features of ENSO's time evolution, the probability distribution function (PDF) of the Niño-3 index from observations and models is displayed in Figs. 3a–d. The observed maximum positive SSTA can reach about 4°C, but the maximum negative SSTA is only about −2°C, which is consistent with the observed positive skewness value of the Niño-3 index (1.02). Although the maximum positive SSTA in all three models are slightly smaller (GFDL-CM4) or similar to the observed (E3SM-1-0 and CESM2), it has a larger probability for the occurrence for a band of warm anomalies ranging from 0.5° to 3.5°C in E3SM-1-0 and CESM2 but not in GFDL-CM4, which is in agreement with the larger standard deviation of the Niño-3 index in E3SM-1-0 and CESM2

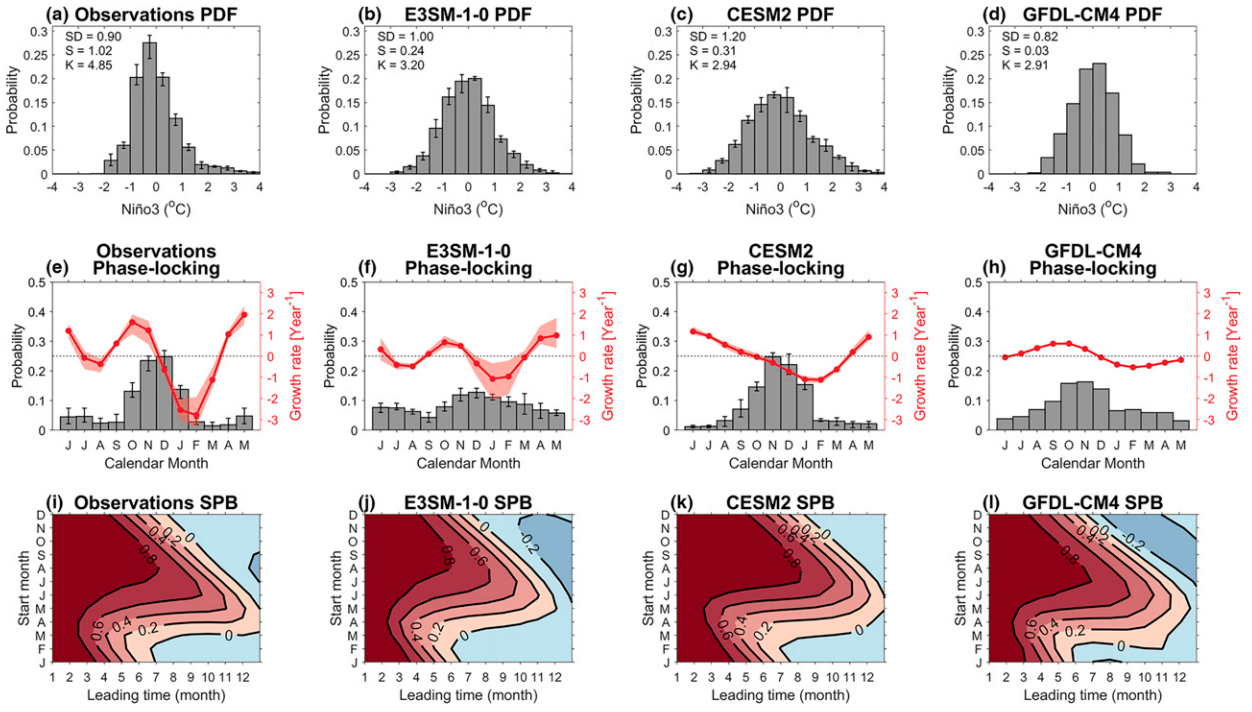

FIG. 3. Statistical features of ENSO's time evolution in observations, E3SM-1-0, CESM2, and GFDL-CM4 for (a)–(d) probability distribution of Niño-3 index for the observations and climate models, (e)–(h) peak phase histogram of ENSO phase–locking (bars) and SST growth rate (curves with dots), and (i)–(l) autocorrelation as a function of the initial calendar month and lag month of Niño-3 index. The mean of SST growth rate is removed in (e)–(h). The vertical lines in (a)–(c) and red shadings in (e)–(g) indicate the minimum and maximum values of the reanalysis datasets or model ensemble members.

(1.00 and 1.20, respectively). The magnitude of the maximum negative SSTA is overestimated in E3SM-1-0 and CESM2 (about −3.0°C) but is similar to the observed SSTA in GFDL-CM4. The probability of the occurrence of cold anomalies from −0.5° to −3°C is higher in E3SM-1-0 and CESM2 than in observations. The results indicate that cold SSTA in E3SM-1-0 and CESM2 is overestimated, and warm SSTA in GFDL-CM4 is underestimated. These are the major causes for the smaller asymmetry of ENSO (skewness value is 0.24, 0.31, and 0.03 in E3SM-1-0, CESM2, and GFDL-CM4, respectively).

The preferred peak month of observed ENSO events occurs in boreal winter (i.e., phase-locking phenomenon) as illustrated by the phase histogram of Niño-3 index in Fig. 3e. The seasonal modulation of ENSO's SST growth rate, which controls the observed phase-locking, is calculated by the seasonal linear inverse model proposed by Chen and Jin (2021) and represented as a dotted curve in Fig. 3e. According to observations, ENSO's preferred peak times tend to appear at the end of the calendar year from November to January, where the seasonal cycle of ENSO's SST growth rate transitions from positive to negative, and it has a strong preference for phase-locking. This strong winter peak phase-locking is a difficult aspect for climate models to simulate realistically—either peaking at the wrong season or showing weak strength of phase-locking (Chen and Jin 2021). E3SM-1-0, CESM2, and GFDL-CM4 all exhibit preferred peak times in boreal winter as shown in observations (Figs. 3f–h). However, the strength of the phase-locking preference is much weaker in E3SM-1-0 and GFDL-CM4 due to the relatively strong semiannual cycle of SST growth rate in E3SM-1-0 and small annual cycle component of SST growth rate in GFDL-CM4. Based on the linear dynamics of ENSO phase-locking, Chen and Jin (2021) demonstrated that the small amplitude of the annual cycle of SST growth rate and strong semiannual cycle in SST growth rate tends to reduce the strength of ENSO phase-locking or yield unrealistic double peaks.

The spring persistence barrier (SPB), which is an obvious observable ENSO property, refers to the rapid decline in ENSO's predictability during the boreal spring. The SPB is represented by the autocorrelation as a function of the initial calendar month and lag month of the Niño-3 index (Figs. 3i–l). Both observations and climate models show that the autocorrelations decline with the increase of lag months and exhibit a strong seasonal dependence, where the autocorrelations decrease significantly across boreal spring. This result indicates that E3SM-1-0, CESM2, and GFDL-CM4 can reasonably reproduce the observed timing of the ENSO SPB that occurs during the boreal spring.

c. *Basic recharge oscillator dynamics*

The recharge oscillator framework argues that the recharge and discharge of equatorial heat content cause the coupled system to oscillate [Eqs. (1) and (2)], and the relationship between eastern Pacific SSTA and western Pacific thermocline

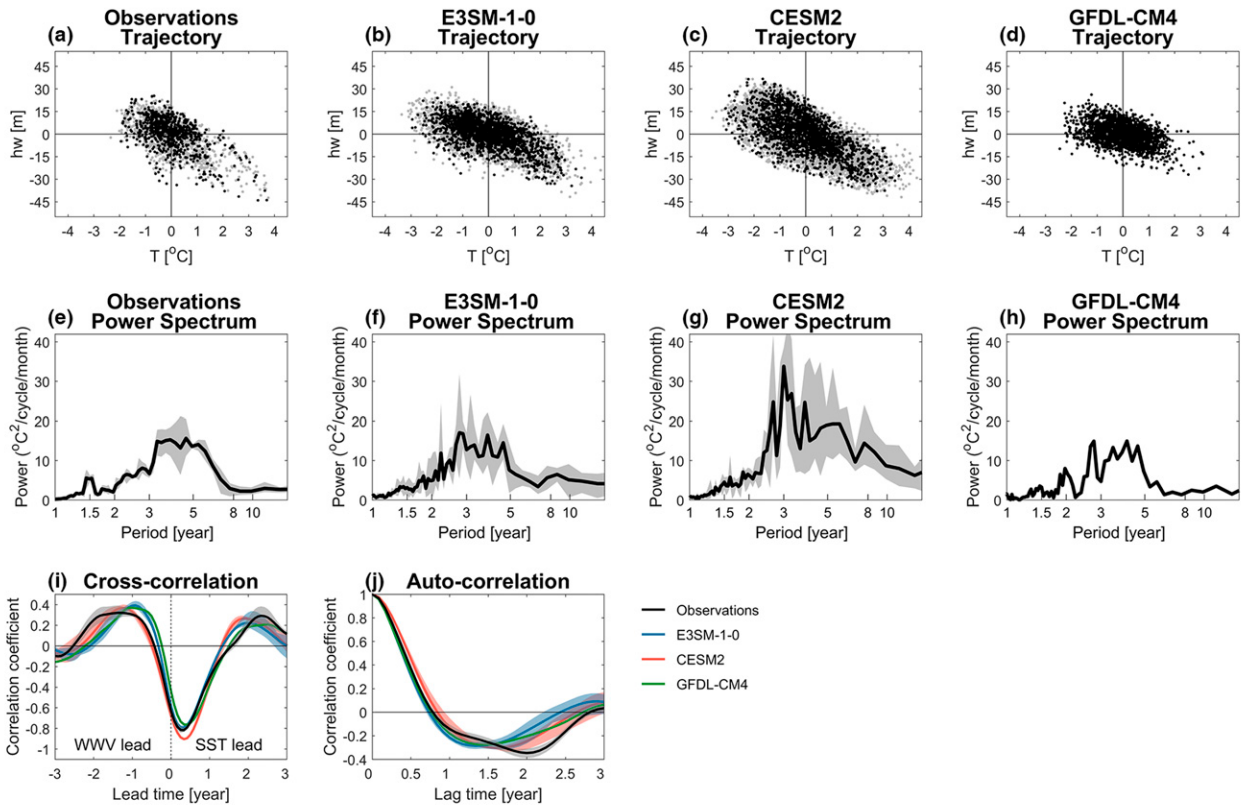

FIG. 4. Basic recharge oscillator dynamics in observations, E3SM-1-0, CESM2, and GFDL-CM4 for (a)–(d) the trajectory on the phase plane of the monthly T_E and h_w, (e)–(h) power spectrum analysis of the Niño-3 index, (i) lagged cross-correlation between T_E and h_w, and (j) autocorrelation function of the Niño-3 index. The black dots represent the ORAS5 in (a) and the r1i1p1f1 model member in (b) and (c). The gray dots denote the SODA331, SODA224, and GODAS in (a) and the r2i1p1f1, r3i1p1f1, and r4i1p1f1 model members in (b) and (c). The shading in (e)–(h) and in (i) and (j) indicates the minimum and maximum values of the reanalysis datasets or model ensemble members. The critical value for a 95% confidence level in (i) is 0.09 for observations and 0.04 for models.

depth anomalies can be illustrated by the trajectory on the phase plane of (T_E, h_w). The trajectory on the phase plane of the observed T_E and h_w (Fig. 4a) exhibits a clockwise elliptical-shaped orbit with significant asymmetry between warm and cold conditions, which comes from the nonlinearity and irregularity of ENSO variability in observations. In contrast, the trajectory of simulated T_E and h_w is more symmetric (Figs. 4b–d), indicating the nonlinearity and irregularity of ENSO variability in the climate models are much smaller than in observations. Moreover, the tilting angle of the simulated trajectory is smaller in E3SM-1-0 and GFDL-CM4, indicating that their amplitude of western Pacific thermocline variability is smaller compared with observations. The maximum response of h_w to T_E is about -6.7 m K^{-1} for E3SM-1-0 and GFDL-CM4, which is much smaller than the observed value and that for CESM2 (maximum regression coefficient is -9.4 and -9.9 m K^{-1}, respectively). To further confirm the relation between SSTA and thermocline depth anomalies, the lagged cross-correlation between T_E and h_w is shown in Fig. 4i. In both observations and climate models, the thermocline depth anomalies at the western Pacific are negatively correlated with the SSTA with a time delay of about 4–5 months, and the maximum positive correlation appears when thermocline depth anomalies lead SSTA about one year.

The power spectrum of the observed Niño-3 index shows a broad maximum with a period ranging between 2 and 7 years, during which the main period is approximately 3.5–6 years (Fig. 4e). The spectrum of E3SM-1-0, CESM2, and GFDL-CM4 is also dominated by an observational period ranging between 2 and 7 years, but the major periods are shorter in the simulations. Another way to characterize ENSO's periodicity is through the autocorrelation function of the Niño-3 index (Fig. 4j). In observations and all model cases, the maximum negative correlation occurs at a lag of 12–30 months, corresponding to the period of about 2–5 years. The lag of the observed maximum negative correlation (~24 months) is longer than all models (12–20 months), indicating that the period of simulations is shorter than the period of observations, which is consistent with the spectrum analysis result.

The above results indicate that the fundamental features of RO dynamics, including the relationship between SSTA and thermocline depth anomalies, and the periodicity of ENSO are well described by the climate models but have some deficiencies.

d. Atmospheric dynamics and thermodynamics response

The spatial structure of the atmospheric response to ENSO's SSTA is the key factor in determining the growth and frequency

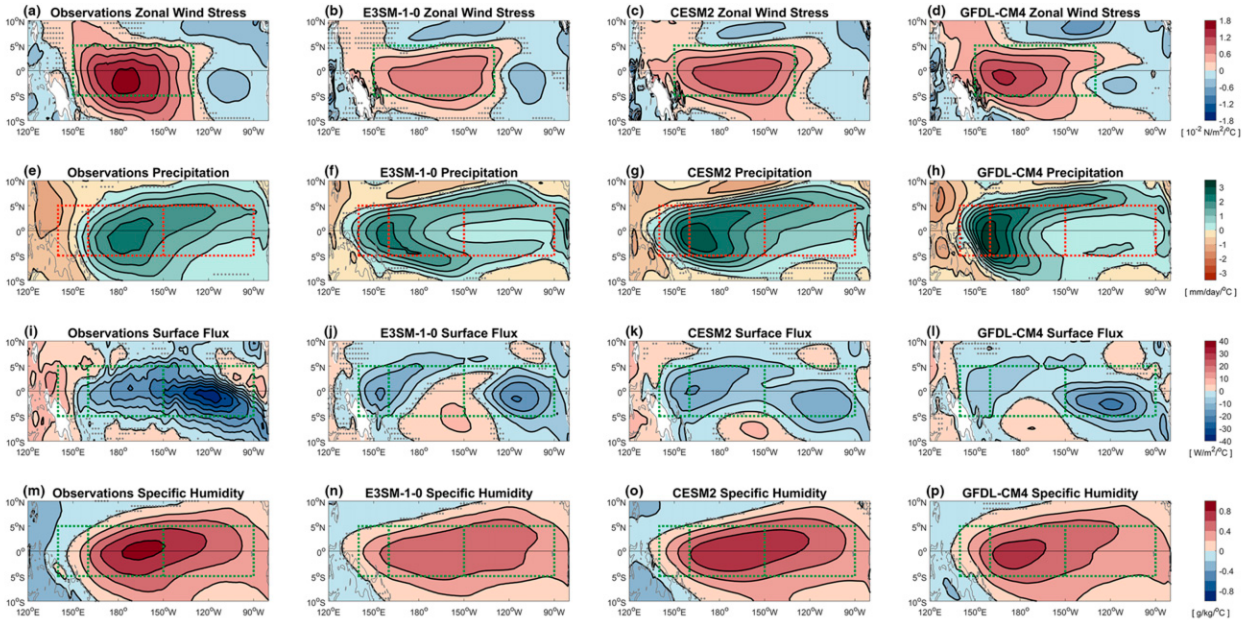

FIG. 5. Atmospheric dynamics and thermodynamics response in observations, E3SM-1-0, CESM2, and GFDL-CM4 for regression of (a)–(d) zonal wind stress, (e)–(h) precipitation rate, (i)–(l) surface heat flux, and (m)–(p) vertical integrated specific humidity from 925 to 400 hPa onto the Niño-3 index. Positive values indicate downward flux in (i)–(l). The rectangles in (a)–(d) indicate the equatorial central–western Pacific region and the three rectangles from west to east in (e)–(p) represent the region for equatorial western Pacific, Niño-4, and Niño-3, respectively. Gray dots indicate the shading values that are not statistically significant at the 95% confidence level.

of ENSO. In this subsection, the atmospheric response in terms of zonal wind stress, precipitation, surface heat flux, and specific humidity is investigated to evaluate models' ENSO dynamic. The spatial patterns of the zonal wind stress anomalies associated with ENSO in observations and models are obtained by regressing the zonal wind stress anomalies onto the Niño-3 index at each grid point (Figs. 5a–d). In observations and all simulations, the pronounced positive feedback of zonal wind stress is mainly in the equatorial central-western Pacific region (150°E–130°W) and slightly shifted to the Southern Hemisphere. However, in all three models the zonal wind stress response is too weak, displaced too far west, and too narrow in the meridional direction, consistent with previous studies (e.g., Wittenberg et al. 2006; Capotondi et al. 2006; Kim et al. 2008; Choi et al. 2013, 2015; Held et al. 2019). The meridional scale and longitudinal location of wind response are important for the amplitude and time scale of ENSO, where the longitudinal location of the wind stress anomalies response can influence the zonal advective feedback and the meridional scale of wind stress response can determine the amount of warm water recharged/discharged to the equator (Capotondi et al. 2006).

The precipitation patterns associated with ENSO are important for determining the extratropical teleconnections. Figure 5e shows the observed precipitation rate anomalies regressed on the Niño-3 index. The center of the positive precipitation anomalies is shown over the central Pacific (170°–160°W); meanwhile, there are negative precipitation anomalies over the equatorial western Pacific (west of 150°E). In the climate models, the center of the positive precipitation anomalies is shifted westward to about 160°E and slightly extends to the Southern Hemisphere (Figs. 5f–h). The zonal shift of the ENSO-related precipitation anomalies is one of the well-known systematic biases in many climate models, which is caused by the equatorial cold bias of mean SST (Wittenberg et al. 2006; Ham and Kug 2012, 2015; Zhang and Sun 2014). In addition, the negative precipitation anomalies retreat to the west of 130°E in E3SM-1-0 and CESM2, and the west of 140°E in GFDL-CM4, which is consistent with the excessive westward extension of the SSTA and zonal wind stress.

The surface heat flux, defined as the sum of shortwave radiative flux, longwave radiative flux, sensible heat flux, and latent heat flux, are dominated by shortwave radiation and latent heat flux in ENSO evolution. The spatial patterns of the surface heat flux anomalies on the Niño-3 index are shown in Figs. 5i–l (positive values indicate downward flux). In observations, the equatorial Pacific is dominated by two regions of upward surface heat flux anomalies (negative values). The first large negative surface heat flux anomalies region is along the equator east of 150°W and extends to 5°–10°S, where the large negative values are primarily contributed by the upward latent heat flux term (see supplemental Fig. 1e in the online supplemental material). More upward heat flux anomalies are located in the Niño-4 region (5°S–5°N, 160°E–150°W), and are mainly caused by the shortwave radiation term related to deep convection (supplemental Fig. 1a). For climate models, the locations of these two upward heat flux regions are farther apart because the deep convection region is farther west in simulations (Figs. 5i–l and supplemental Figs. 1b–d). In the eastern Pacific, although the total heat flux anomalies are dominated by the latent heat term, the bias of surface heat flux anomalies between simulations and observations is caused by the shortwave radiation

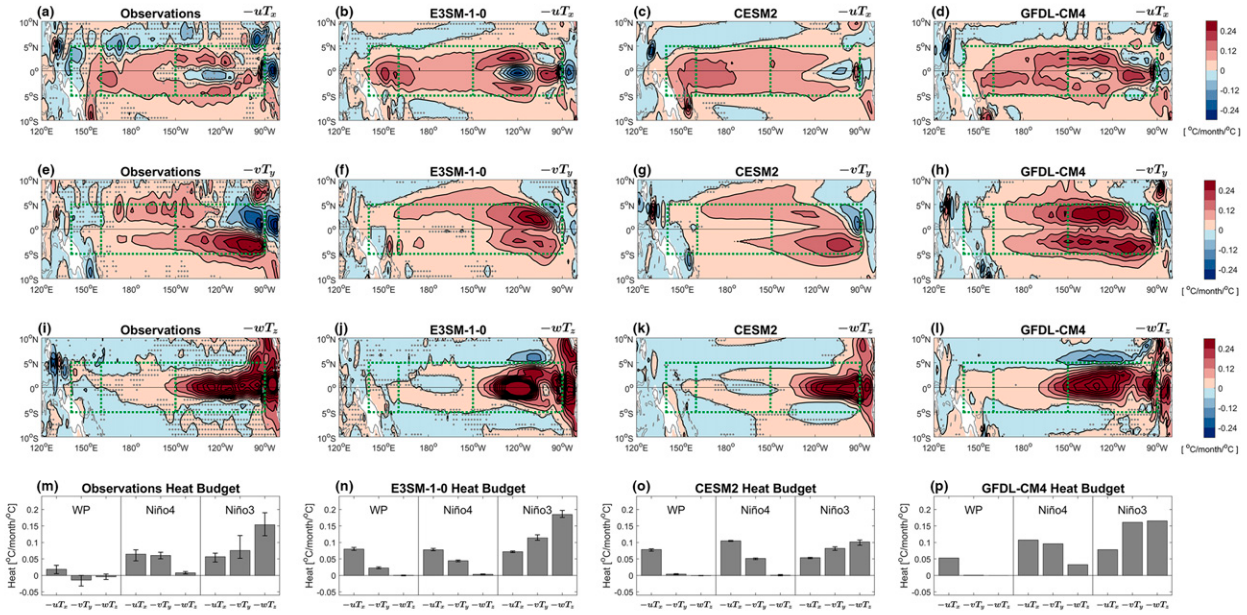

FIG. 6. Heat budget analysis of ocean mixed layer in observations, E3SM-1-0, CESM2, and GFDL-CM4 for regression of (a)–(d) zonal temperature advection, (e)–(h) meridional temperature advection, and (i)–(l) vertical temperature advection onto Niño-3 index with a lag of 3 months. (m)–(p) The area average of each term in the Niño-3, Niño-4, and western Pacific regions. The three rectangles from west to east in (a)–(l) represent the regions for the equatorial western Pacific (WP), Niño-4, and Niño-3, respectively. The vertical lines in (m)–(p) indicate the minimum and maximum values of the members. Gray dots indicate the shading values that are not statistically significant at the 95% confidence level.

term (supplemental Figs. 1q–t). In spite of the deep convection in the eastern Pacific is relatively weak, the shortwave radiative flux anomalies are largely affected by low-level cloud, which is not captured well by most models (Lloyd et al. 2009, 2012).

The atmospheric moisture is the key in thermodynamics component to control the ENSO-induced precipitation. The vertical integrated specific humidity anomalies from 925 to 400 hPa are shown in Figs. 5m–p. In observations, the increased specific humidity anomalies are shown over the central Pacific with the center at 180°–150°W. In contrast, the center of the simulated positive specific humidity anomalies moves to the west, which corresponds to the westward shift of simulated SSTA and precipitation anomalies.

The above analysis of atmospheric response to ENSO SSTA suggests that E3SM-1-0, CESM2, and GFDL-CM4 all underestimate ENSO's positive dynamic feedback (through zonal wind stress) and thermodynamic damping (mainly through the shortwave component in the total surface heat flux), and the opposite biases in dynamic and thermodynamic feedbacks will at least partially compensate each other in the total BJ index (details will be discussed in section 4b).

4. ENSO dynamics and feedbacks

a. Mixed layer heat budget analysis

In this section, the heat budget analysis of the ocean mixed layer is used to diagnose the contribution of different ocean processes to SSTA in the Niño-3 region and the causes of the excessive westward extension of ENSO SSTA in climate models. Figure 6 illustrates the spatial patterns of zonal, meridional, and vertical advection terms associated with ENSO, and the area average of each term in the Niño-3 region (5°S–5°N, 150°–90°W), Niño-4 region (5°S–5°N, 160°E–150°W), and far western Pacific (WP; 5°S–5°N, 140°–160°E), which is shown with a bar diagram. Because the tendency of SSTA leads SSTA about 3 months, in this section each tendency term in Eq. (5) will be regressed onto Niño-3 index with a lag of 3 months.

In the Niño-3 region, where the ENSO-related SST variability is strongest, the dominant process is vertical advection in observations and climate models (Figs. 6m–p), which is consistent with previous studies (An and Jin 2001). However, the contribution of meridional advection is larger in simulations due to the underestimated negative meridional advection of the northern branch, especially in GFDL-CM4 (Figs. 6e–h). For the Niño-4 region, the warming of SSTA is mainly controlled by the zonal advection, followed by meridional advection (Figs. 6i–l). The small contribution of vertical advection in the Niño-4 region is caused by the weak vertical gradient of SSTA in the mixed layer (Figs. 7e–h). In the WP region, where the SST variability is small, the zonal advection in the climate models is much larger than that in observations (Figs. 6m–p). In climate models, the positive zonal advection can extend to 140°E (Figs. 6b–d); however, in observations, the positive zonal advection only extends to 150°E and becomes a negative value at the west of 150°E (Fig. 6a).

To further analyze the contribution of vertical advection to developing SSTA in Niño-3 region, the separated terms of

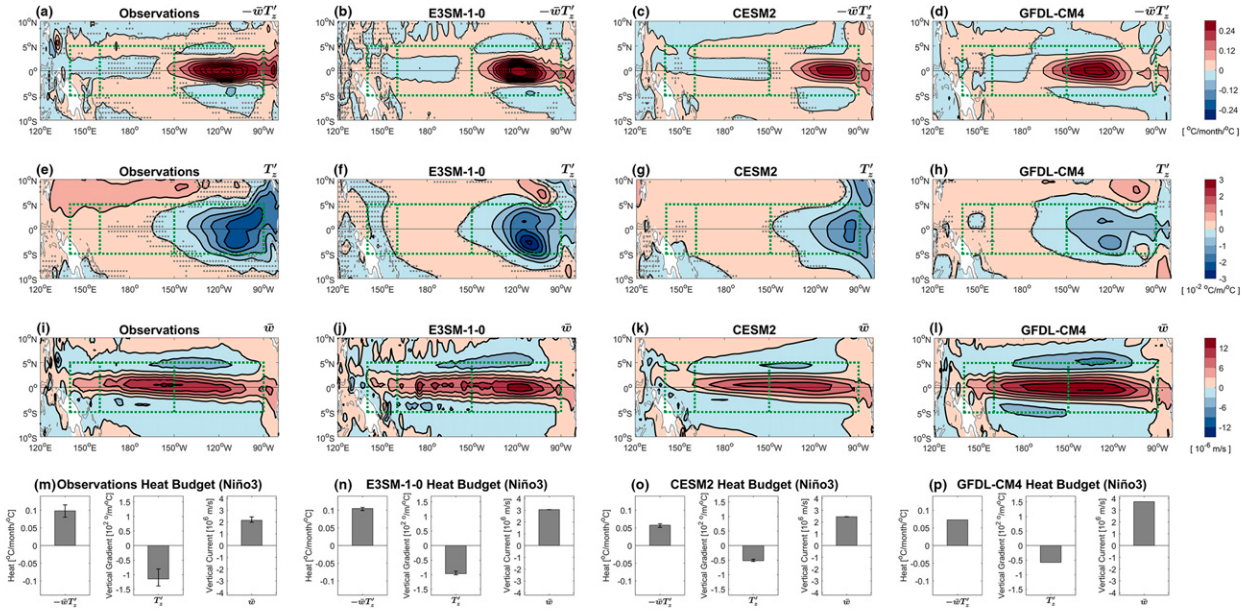

FIG. 7. The separated terms of vertical temperature advection in observations, E3SM-1-0, CESM2, and GFDL-CM4 for (a)–(d) regression vertical advection of anomalous temperature by mean currents onto Niño-3 index with a lag of 3 months, (e)–(h) regression of vertical temperature gradient anomalies onto Niño-3 index with a 3-month lag, and (i)–(l) climatology of the vertical current. (m)–(p) The area average of each term in the Niño-3 region. The three rectangles from west to east in (a)–(l) represent the region for equatorial western Pacific, Niño-4, and Niño-3, respectively. The vertical lines in (m)–(p) indicate the minimum and maximum values of the members. Gray dots indicate the shading values that are not statistically significant at the 95% confidence level.

vertical advection—advection of temperature anomalies by the mean current $[-\overline{w}(\partial T'/\partial z)]$ and advection of mean temperature by anomalous currents $[-w'(\partial \overline{T}/\partial z)]$—are shown in Figs. 7 and 8. Although both processes contribute significantly to the SSTA tendency in observations (Figs. 7m and 8m), the advection of temperature anomalies by the mean current (i.e., thermocline feedback) is much larger than the advection of mean temperature by anomalous currents (i.e., upwelling or vertical advective feedback). For E3SM-1-0, the amplitude of thermocline feedback is as large as the observations (Fig. 7b); however, in CESM2 and GFDL-CM4 the thermocline feedback is smaller than observed (Figs. 7c,d), mainly because of the weaker anomalous vertical temperature gradient (Figs. 7g,h). As shown in Fig. 8, the amplitude of vertical advective feedback in E3SM-1-0 and GFDL-CM4 is greater than observations (Figs. 8m,n,p) due to stronger mean vertical temperature gradient and vertical current anomalies (Figs. 8f,h). In CESM2 the weaker mean vertical temperature gradient (Fig. 8g) and vertical current anomalies (Fig. 8k) result in small vertical advective feedback (Fig. 8o). As a result, the amplitude of the total vertical advection in the Niño-3 region is as large as the observations in E3SM-1-0 and GFDL-CM4, but much smaller in CESM2 due to the weaker thermocline feedback and vertical advective feedback (Figs. 6m–p).

Next, the causes of the uncommon warming of ENSO-related SSTA over the WP region (5°S–5°N, 140°–160°E) in climate models are investigated. The spatial patterns of ENSO-related surface heat flux show that due to the westward shift of deep convection, the ocean surface heat flux loss in the far western Pacific region is higher in simulations than in the observations (supplemental Fig. 2). That is, the surface heat flux term is not the main contributor to the westward extension of simulated SSTA, but is mainly determined by zonal advection as shown in Fig. 6. To further investigate the difference in the zonal advection process between observations and simulations, the separated terms of zonal advection—advection of mean temperature by anomalous currents $[-u'(\partial \overline{T}/\partial x)]$ and advection of temperature anomalies by mean current $[-\overline{u}(\partial T'/\partial x)]$—are shown in Figs. 9 and 10. For zonal advection of mean temperature by anomalous currents $[-u'(\partial \overline{T}/\partial x)]$, similar to the total zonal advection, the positive zonal advection can extend to 140°E in the models but can only extend to 150°E in observations (Figs. 9a–d). This bias in the WP is caused by the climatology of the zonal temperature gradient (Figs. 9m–p), which has a positive gradient west of 150°E in observations but not in models (Figs. 9e–h). In climate models, the maximum equatorial mean SST is located near the western boundary of the Pacific; however, the observed maximum equatorial mean SST is about 150°E, which turns the sign of zonal gradient west of 150°E (Fig. 1). Despite the fact that the observed eastward zonal current anomalies are large in the WP region, the positive zonal gradient of mean SST west of 150°E makes the advection of mean temperature by anomalous currents in the observations smaller than simulated. For zonal advection of anomalous temperature by mean currents $[-\overline{u}(\partial T'/\partial x)]$, the center of the maximum positive zonal advection in the observations is located at about 165°E; however, it extends more westward in the simulations (Figs. 10a–d), causing the positive

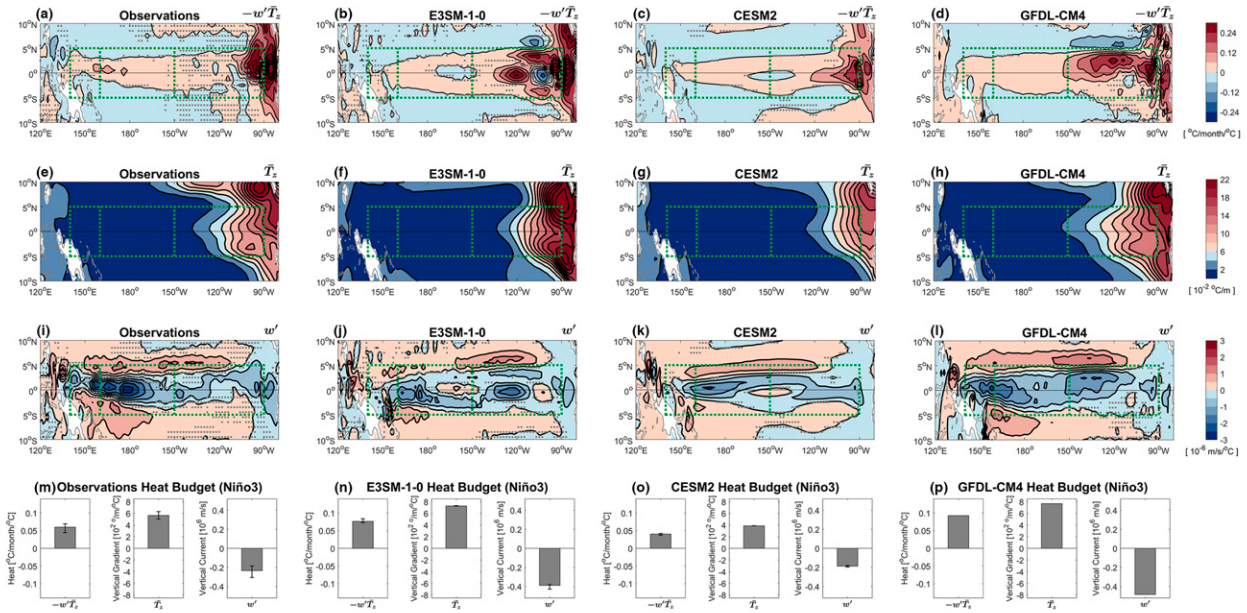

FIG. 8. The separated terms of vertical temperature advection in observations, E3SM-1-0, CESM2, and GFDL-CM4 for (a)–(d) regression vertical advection of mean temperature by anomalous currents onto Niño-3 index with a lag of 3 months, (e)–(h) climatology of the vertical temperature gradient, and (i)–(l) regression of vertical current anomalies onto Niño-3 index with a 3-month lag. (m)–(p) The area average of each term in the Niño-3 region. The three rectangles from west to east in (a)–(l) represent the region for equatorial western Pacific, Niño-4, and Niño-3, respectively. The vertical lines in (m)–(p) indicate the minimum and maximum values of the members. Gray dots indicate the shading values that are not statistically significant at the 95% confidence level.

zonal advection in the WP to be larger in models than observed (Figs. 10m–p). In simulations, the edge of ENSO's SSTA is shifted to the WP region (supplemental Fig. 3), resulting in the center of the maximum positive value of anomalous zonal SST gradient being more westward than that that in observations (Figs. 10e–h). Additionally, the simulated mean westward zonal current in the WP is stronger than in the observed (Figs. 8i–l). In summary, in climate models, due to the higher anomalous zonal temperature gradient and stronger mean westward zonal current in the WP region, the zonal advection of anomalous temperature by mean currents in climate models is larger than that in observations.

According to the above results, this excessive westward extension of ENSO-related SSTA in model simulations is the result of the increased zonal temperature advection, which is mainly due to the stronger climatological westward zonal current, more negative climatological zonal temperature gradient, and larger positive anomalous zonal temperature gradient. More simply, this could be described as a westward expansion of the "cold tongue regime" in the climate models, which displaces the region of strong zonal advection and associated zonal advective feedbacks (Jiang et al. 2021).

b. *Bjerknes stability and Wyrtki periodicity*

As mentioned in section 3d, both SST–wind coupling and thermodynamic radiative feedbacks are underestimated in climate models. To evaluate ENSO's growth rate and periodicity in both observations and model simulations, and to understand the contribution of the compensation between dynamic and thermodynamic feedbacks to ENSO's growth rate, the Bjerknes stability (Jin et al. 2006) index and Wyrtki periodicity (Lu et al. 2018) index (herein BJ index and WJ index, respectively) are adopted. As shown in Fig. 11a, the BJ indices for both observations and climate models yield an ENSO growth rate from -0.3 to 0.01 yr^{-1}, which indicates that ENSO coupled dynamics are very close to criticality (Jin et al. 2020). However, both the dynamic part and thermodynamic part of growth rate in the three climate models are much weaker than those in observations (Figs. 11b,c). The strong compensation between dynamic and thermodynamic feedbacks contributes to a similar neutral growth rate, which partly explains the similar ENSO amplitude. This result indicates that the systematic bias persists from CMIP3 (Kim and Jin 2011) and CMIP5 (Kim et al. 2014) to CMIP6. The weaker zonal wind stress response to SSTA in climate models would contribute to an underestimation of zonal advective and thermocline feedbacks, resulting in a weaker dynamics part of growth rate (Kim et al. 2014). At the same time, insufficient convective cloud shading of the equatorial eastern Pacific SSTA during warm events would underestimate the upward surface heat flux, leading to a weaker thermodynamic part of growth rate (Figs. 5i–l). In other words, the bias in atmospheric response of ENSO and simulation of low-level cloud remains one of the biggest challenges for state-of-the-art climate models.

As shown in Fig. 11d, the WJ index yields a period of 4.3 years for observations but about 3.5 years for the three climate models,

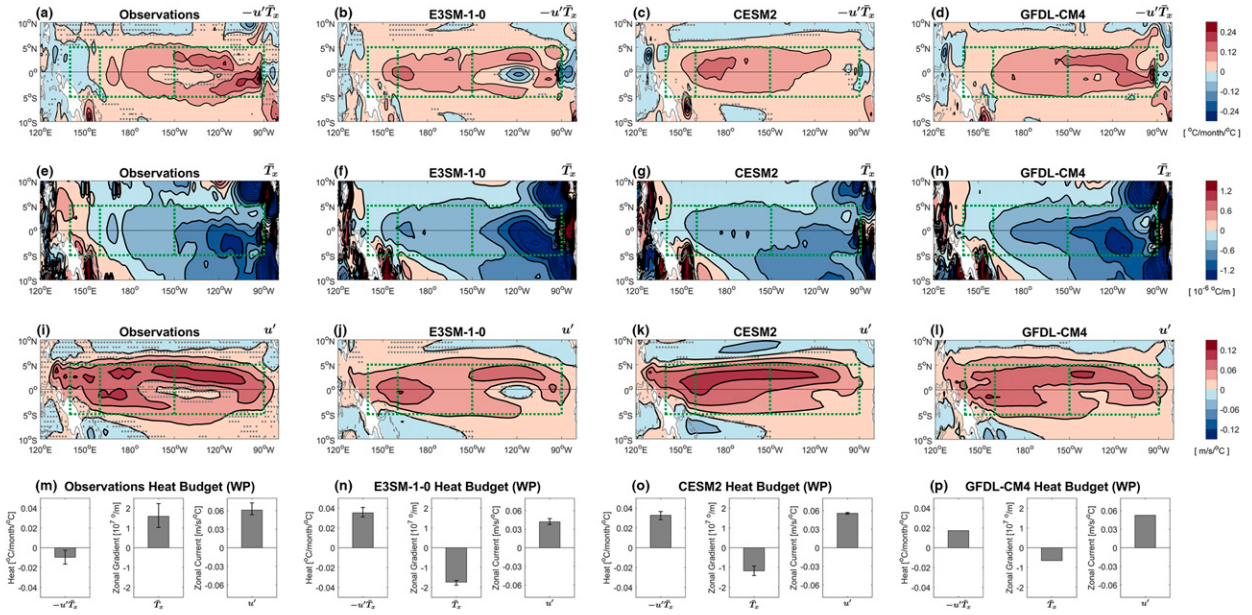

FIG. 9. The separated terms of zonal temperature advection in observations, E3SM-1-0, CESM2, and GFDL-CM4 for (a)–(d) regression zonal advection of mean temperature by anomalous currents onto Niño-3 index with a lag of 3 months, (e)–(h) climatology of the zonal temperature gradient, and (i)–(l) regression of zonal current anomalies onto Niño-3 index with a 3-month lag. (m)–(p) The area average of each term in the western Pacific region. The three rectangles from west to east in (a)–(l) represent the region for equatorial western Pacific, Niño-4, and Niño-3, respectively. The vertical lines in (m)–(p) indicate the minimum and maximum values of the members. Gray dots indicate the shading values that are not statistically significant at the 95% confidence level.

which is consistent with the previous analysis of power spectrum and autocorrelation. According to the WJ index [Eq. (4)], the shorter period in the models is mainly caused by the much stronger coefficient of SST phase-transition F_1 in all three models (Fig. 11e) and the larger thermocline phase-transition rate F_2 in CESM2 and GFDL-CM4. The stronger SST phase-transition F_1 in models may be due to the bias in the meridional scale and longitudinal location of the ENSO wind response (Figs. 5a–d). The narrower meridional scale of zonal wind stress anomalies excites faster off-equatorial Rossby waves close to the equator, hastening the thermocline adjustment and shortening the ENSO period (Kirtman 1997; Jin 1997b; Capotondi et al. 2006; Jin et al. 2020). The westward displacement of the zonal wind stress anomalies, and the associated zonal current response, shifts the zonal advective feedback westward, weakening the zonal advective feedback in the eastern Pacific and accelerating the transition of ENSO (An and Wang 2000; Capotondi et al. 2006). Thus, both the narrow meridional scale and the westward displacement of the simulated ENSO wind response in the three models may contribute to the stronger SST phase-transition rate F_1 and a shorter ENSO period.

c. *Nonlinearity of the equatorial Pacific Ocean*

An underestimate of ENSO asymmetry remains a common problem in recently released CMIP6 models. Hayashi et al. (2020) demonstrated that the asymmetry of ENSO is largely proportional to subsurface NDH. To investigate the cause of the weak asymmetry in E3SM-1-0, CESM2, and GFDL-CM4, the subsurface NDH is derived from the nonlinear temperature advection terms as

$$\mathrm{NDH} = -u'\frac{\partial T'}{\partial x} - v'\frac{\partial T'}{\partial y} - w'\frac{\partial T'}{\partial z}. \tag{6}$$

The regressed equatorial NDH and nonlinear temperature advection terms onto the Niño-3 index are shown in Fig. 12 and supplemental Fig. 4. In the observations, there is a significant positive subsurface NDH along the equatorial Pacific thermocline over the central-eastern Pacific (Fig. 12a). This positive NDH reduces the cooling subsurface temperature tendency during the transition from El Niño to La Niña, and enhances the asymmetry of ENSO (Hayashi and Jin 2017). The observed subsurface NDH is mainly caused by the nonlinear zonal temperature advection (Fig. 12e), where strong zonal temperature gradient and westward zonal current anomalies (weakened equatorial undercurrent by the westerly winds) along the thermocline are present (Figs. 12i,m). In contrast, the contribution of nonlinear meridional and vertical advection to the NDH is much smaller (supplemental Figs. 4a,e). However, in the climate models, the weak nonlinear zonal temperature advection leads to too-weak subsurface NDH (Figs. 12b–d and 12f–h), accompanied by the weak skewness of ENSO. All simulations fail to reproduce the anomalous westward zonal current anomalies and GFDL-CM4 even presented eastward zonal current anomalies (Figs. 12n–p). The positive zonal temperature gradient anomalies along the thermocline are also weak (Figs. 12j–l) in models.

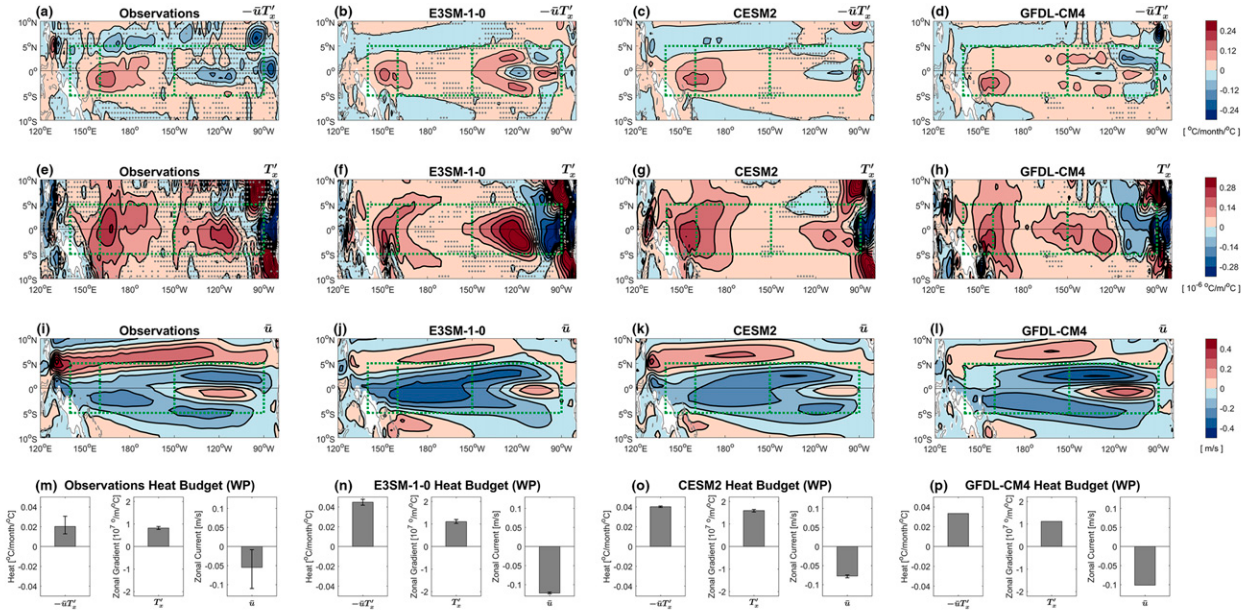

FIG. 10. The separated terms of zonal temperature advection in observations, E3SM-1-0, CESM2, and GFDL-CM4 for (a)–(d) regression zonal advection of anomalous temperature by mean currents onto Niño-3 index with a lag of 3 months, (e)–(h) regression of zonal temperature gradient anomalies onto Niño-3 index with a 3-month lag, and (i)–(l) climatology of the zonal current. (m)–(p) The area average of each term in the western Pacific region. The three rectangles from west to east in (a)–(l) represent the region for equatorial western Pacific, Niño-4, and Niño-3, respectively. The vertical lines in (m)–(p) indicate the minimum and maximum values of the members. Gray dots indicate the shading values that are not statistically significant at the 95% confidence level.

The failure to simulate ENSO-related subsurface zonal current anomalies and zonal temperature gradient anomalies resulted in a reduction of nonlinear advective processes below the mixed layer and a too-weak ENSO asymmetry in climate models. In fact, the inability to simulate zonal current and zonal temperature gradient anomalies might not be a direct problem of the ocean model, but could be due to the atmospheric wind response or coupled air–sea biases that influence

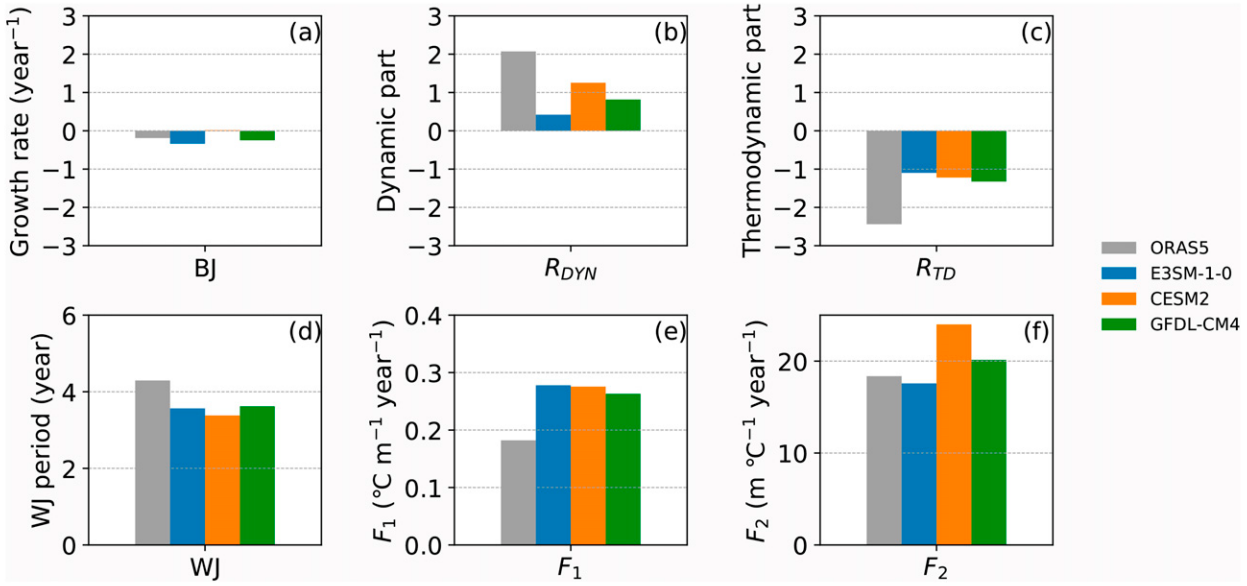

FIG. 11. The Bjerknes stability and Wyrtki periodicity indices in observations, E3SM-1-0, CESM2, and GFDL-CM4 models for (a) the Bjerknes stability index $(R_{\mathrm{DYN}} + R_{\mathrm{TD}})/2$, (b) its dynamic part R_{DYN}, (c) its thermodynamic part R_{TD}, (d) the Wyrkti period $2\pi/\sqrt{F_1F_2 - (R+r)^2/4}$, (e) the SST phase-transition rate F_1, and (f) the thermocline phase-transition rate F_2.

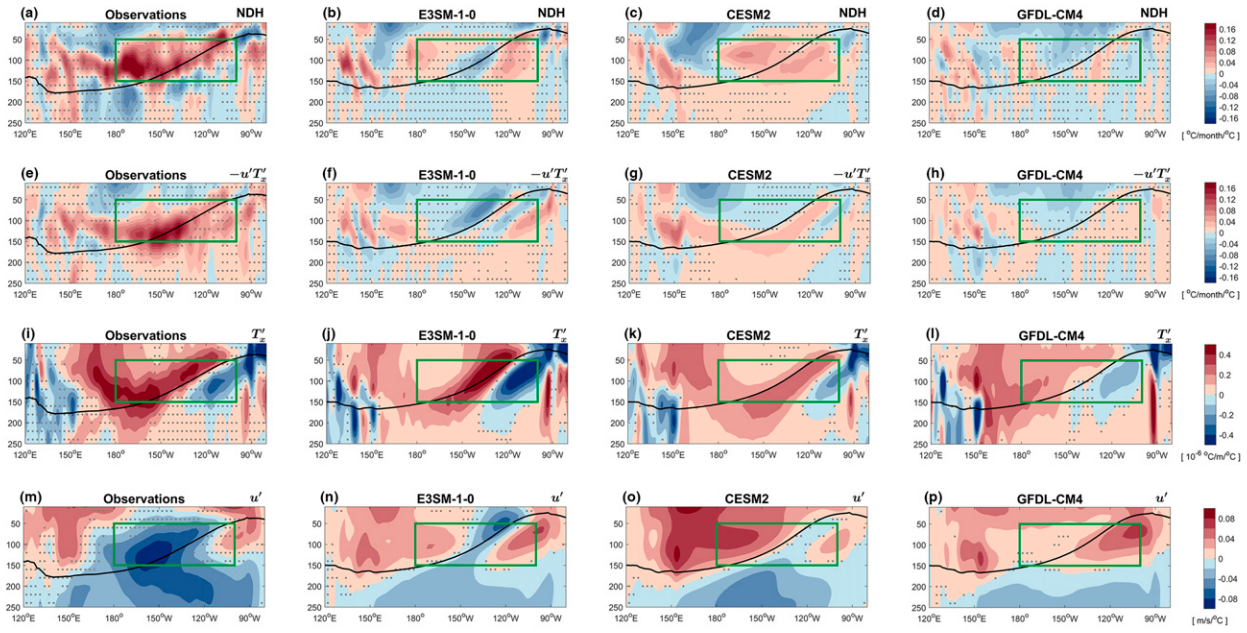

FIG. 12. Nonlinearity of the equatorial Pacific Ocean (2°S–2°N) in observations, E3SM-1-0, CESM2, and GFDL-CM4 for the regression of (a)–(d) subsurface NDH anomalies, (e)–(h) nonlinear zonal advective anomalies, (i)–(l) zonal temperature gradient anomalies, and (m)–(p) zonal current anomalies onto Niño-3 index. The green rectangles represent the region where the subsurface NDH effectively influences the asymmetry of SSTA. The black curves indicate the climatology of thermocline (D20). Gray dots indicate the shading values that are not statistically significant at the 95% confidence level.

the wind response. As shown in Held et al. (2019), the simulated ENSO-related wind response looks much better in AMIP simulations. Hayashi et al. (2020) also argued that errors in the SST–wind coupling contribute to biases in subsurface NDH. The weaker ENSO wind responses in E3SM-1-0, CESM2, and GFDL-CM4 (Figs. 5a–d) cause weaker westward zonal current anomalies, resulting in insufficient subsurface NDH.

5. Conclusions and discussion

The recent state-of-the-art climate models are able to realistically simulate basic features of ENSO in terms of dominant time scale, amplitude, spatial patterns, phase-locking, spring prediction barrier, and fundamental recharge oscillator dynamics. However, several aspects of ENSO are still not satisfactorily represented in the climate models, and may achieve realistic levels of ENSO activity for the wrong reasons. In this study, we provide a comprehensive and systematic analysis of ENSO in the historical simulation of E3SM-1-0, CESM2, and GFDL-CM4.

For the time series structure of ENSO, all three models exhibit a dominant period ranging between 2 and 7 years, which is the same as the observed time scale, but the major periods are shorter in the models. According to the WJ analysis, the shorter period in climate models mostly arises from the much stronger ENSO SST phase transition rate F_1, which is caused by the narrower meridional scale and westward displacement of the zonal wind stress response to SSTAs, in the models relative to observations. Although both observations and model simulations show that the preferred peak month of ENSO events occurs in boreal winter, the strength of phase-locking preference is much weaker in E3SM-1-0 and GFDL-CM4. This is due to the relatively strong semiannual cycle of SST growth rate in E3SM-1-0 and small annual cycle component of SST growth rate in GFDL-CM4. Our results also indicate that these models also can well capture the fundamental features of RO dynamics, and reproduce the relationship between SSTA and thermocline depth anomalies in the ENSO evolution.

Observed ENSO has the most significant interannual climate signal in the tropical SSTA and its largest SST variability manifested in the eastern Pacific and off the coast of Peru. Although the ENSO-related SSTA in E3SM-1-0, CESM2, and GFDL-CM4 also shows an obvious signal in the eastern Pacific, the detailed spatial features of the SSTA variability have differences from the observed. The amplitude of SSTA in GFDL-CM4 is closer to the observed values in the central-eastern tropical Pacific but is overestimated in E3SM-1-0 and CESM2. In E3SM-1-0 and GFDL-CM4, the significant standard deviations are achieved around 180° and 170°W, respectively, which are similar to the observed variability (~170°W), while in CESM2 it extends too westward (near 160°E). Moreover, the region of the large variability is tightly confined to the equator around 2°S–2°N in observations but the meridional extension is much wider in all climate models, especially in CESM2. By composite analysis and calculating skewness, we found that all three models underestimated the positive asymmetry of SSTA in the eastern Pacific, where the observed SSTA are skewed toward warm events, indicating that these models cannot capture the observed ENSO nonlinearities.

The models fail to simulate ENSO-related subsurface zonal current anomalies and zonal temperature gradient anomalies, which resulted in a reduction of nonlinear advective processes below the mixed layer and a too-weak ENSO asymmetry in climate models.

Another notable bias of ENSO-related SSTA variability is that the edge of SSTA in model simulations extends more westward than the observed result. There is a negative SSTA in the observations during El Niño in the western Pacific (5°S–5°N, 140°–160°E), while the positive SSTA extends too far into the western Pacific in all three models. The results of heat budget analysis indicate that this uncommon warming SSTA over the western Pacific region in models is the result of the increased zonal temperature advection, which is mainly contributed by the stronger climatological westward zonal current, more negative climatological zonal SST gradient, and larger positive zonal SSTA gradient. Associated with the excessive westward extension of ENSO-related SSTA, the atmospheric responses including precipitation, surface heat flux, and specific humidity all shift farther west than observed. Previous studies suggested that this bias comes from the increased intensity of the eastern Pacific cold tongue, which suppresses the local convection over the eastern Pacific due to the decrease of total SST, resulting in an atmospheric deep convection confined to the central-western Pacific (Ham and Kug 2015). Indeed, there is a strong cold bias of mean SST in E3SM-1-0 and GFDL-CM4—but there is no significant cold SST bias in CESM2, which instead has obvious warm SST biases in the cold tongue region and western Pacific. He et al. (2018) and Izumo et al. (2020) suggested that compared to SST, the *relative SST* (RSST; defined as SST minus its tropical mean) is more closely linked to the interannual variations of tropical convection, since the tropical mean SST largely sets the convective threshold (Johnson and Xie 2010). In CESM2, the higher tropical mean SST in CESM2 establishes a higher threshold of deep convection. After removing the tropical Pacific mean SST, there is a cold bias of RSST over central/eastern Pacific in CESM2 (supplemental Fig. 5c). This cold relative SST bias impedes the eastward displacement of deep convection in CESM2, displacing the simulated atmospheric response west of the observed response. Further research is needed to investigate the effect of the excessive westward extension of the SSTA and associated atmospheric response on ENSO's teleconnections.

Our analysis of coupled dynamics revealed significant biases in simulating ENSO feedback processes, in particular the zonal wind and surface heat flux responses. E3SM-1-0, CESM2, and GFDL-CM4 all underestimate the ENSO positive dynamic feedback (due to insufficient zonal wind stress responses to SSTA) and thermodynamic damping (due to insufficient convective cloud shading of equatorial eastern Pacific SSTA during warm events). The results of BJ analysis indicate that the opposite biases in dynamic and thermodynamic feedbacks will compensate each other to obtain the correct ENSO SST growth rate or amplitude for the wrong reason. How to achieve a realistic ENSO simulation through the correct representation of these feedbacks, rather than by compensating for errors, remains one of the biggest challenges for state-of-the-art climate models. The key processes of controlling the error compensations in dynamic and thermodynamic coupled feedbacks for ENSO amplitudes in climate models must be further studied.

Many of model biases exhibited in the simulated ENSO are associated with equatorial Pacific cold tongue, which is too cold and extends too far west. Our results showed that the cold tongue bias in E3SM-1-0 and GFDL-CM4 is accompanied by a too-strong upwelling, as also found by Siongco et al. (2020), where the cold bias is associated with too-strong vertical advection and easterly wind stress over the eastern equatorial region. Moreover, EAM and CAM6, the atmosphere models used in E3SM-1-0 and CESM2 respectively, are very similar in terms of the model physical parameterizations for aerosols, clouds, convection, radiation, and turbulence. Therefore, the differences seen in these two models largely reflect the differences in ocean and ocean–atmosphere coupling.

CESM2 and GFDL-CM4 have improved the representation of ENSO compared to their predecessor models. CESM2 simulates many aspects of the ENSO better than CCSM4 and CESM1, including its time scales, pattern of atmospheric response, and associated teleconnections (Danabasoglu et al. 2020; Capotondi et al. 2020b; Planton et al. 2021). Compared to previous GFDL models (GFDL-CM2.0, GFDL-CM2.1 and GFDL-CM3), GFDL-CM4 has more realistic ENSO amplitudes, time scales, phase-locking, atmospheric response patterns, SST–wind feedbacks, and teleconnections (Held et al. 2019; Wittenberg et al. 2006; Chen and Jin 2021; Planton et al. 2021). Despite these improvements in ENSO performance, the newer models still have some shortcomings, including a shorter ENSO period, weaker ENSO asymmetry, and westward shift of the ENSO SSTA pattern and atmospheric responses relative to observations. The models also exhibit error compensations between ENSO's dynamic and thermodynamic coupled feedbacks.

In addition to the above limitation of the ENSO representation, several aspects of ENSO remain to be investigated in the climate models. A number of studies demonstrated that the Madden–Julian oscillation (MJO) and westerly wind bursts (WWBs) significantly impact ENSO evolution (Kessler et al. 1995; Kleeman and Moore 1997; Moore and Kleeman 1999; Kessler 2001; Perigaud and Cassou 2000; Yu et al. 2003; Lengaigne et al. 2004; McPhaden 2004; Zavala-Garay et al. 2008). There is also evidence to suggest that the MJO and WWBs can be modulated by ENSO (Zhang and Gottschalck 2002; Yu et al. 2003; Eisenman et al. 2005; Gebbie et al. 2007; Hendon et al. 2007; Kug et al. 2009; Sooraj et al. 2009). Numerical studies show that the state-dependent stochastic forcing plays a critical role in the excitation, amplification, and terminations of ENSO events and generates diverse behaviors of ENSO. The ENSO–MJO/WWB interaction is also considered important for ENSO nonlinearity and triggering extreme events. In the equatorial eastern Pacific, the tropical instability waves (TIWs) are another source of ENSO asymmetry. TIWs are generated by meridional shear instabilities associated with strong near-equatorial currents (Philander 1978; Cox 1980) and baroclinic instability caused by the upper-ocean temperature meridional gradient (Hansen and Paul 1984; Wilson and Leetmaa 1988; Yu et al. 1995). TIW-induced heat transport anomalies can damp ENSO's SSTA over the eastern Pacific (Xue et al. 2020). TIWs are more suppressed during El Niño

but more active during La Niña, which leads to stronger damping in La Niña than El Niño and results in observed ENSO asymmetry. However, the climate models mostly underestimate the ENSO–MJO/WWB and ENSO–TIW interactions and need to be further examined.

Furthermore, the spatial complexity of ENSO (Timmermann et al. 2018) is not considered in this study. Some ENSO events are characterized by SSTAs that peak in the eastern Pacific and so are referred to as EP events, while others exhibit peak SSTAs in the central Pacific and so are known as CP events (Kao and Yu 2009). Currently the dynamics of the RO framework and BWJ analysis are amenable only to the EP events; the RO framework will need to be further developed to accommodate analysis of the CP events.

This study suggests that it is important to capture the correct underlying ENSO feedbacks, not just the salient features, in order to ensure reliable sensitivities, predictions, and projections (e.g., Stevenson et al. 2021; Ding et al. 2020; Chen et al. 2017; DiNezio et al. 2012). We can improve the ENSO metrics by adding more dynamic process diagnostics (e.g., the CLIVAR ENSO Metrics Package; Planton et al. 2021). Several aspects of ENSO simulation are still to be investigated in the climate models. The background biases in models need to be reduced by improving the resolution and physical parameterizations (e.g., Griffies et al. 2015; Wittenberg et al. 2018) and using coping strategies like bias corrections (Ray et al. 2018). Moreover, in order to better calibrate the model results, we must improve observations and reanalysis to reduce the uncertainty (e.g., the TPOS2020 project; Cravatte et al. 2016; Kessler et al. 2019).

Acknowledgments. The authors thank all colleagues and students who contributed to this study. Fei-Fei Jin, Han-Ching Chen, and Sen Zhao were supported by U.S. NSF Grant AGS-1813611 and Department of Energy Grant DE-SC0005110. The work at LLNL was supported as part of the Energy Exascale Earth System Model (E3SM) project, funded by the U.S. Department of Energy, Office of Science, Office of Biological and Environmental Research and was performed under the auspices of the U.S. Department of Energy by Lawrence Livermore National Laboratory under Contract DE-AC52-07NA27344. We also appreciate SOEST for their editorial support (this is SOEST Contribution Number 11420).

Data availability statement. All datasets used in this research can be accessed via the following websites: ORAS5 at https://www.ecmwf.int/en/forecasts/dataset/ocean-reanalysis-system-5/; SODA331 and SODA224 at https://www.soda.umd.edu/; GODAS at https://www.cpc.ncep.noaa.gov/products/GODAS/; ERA5 at https://www.ecmwf.int/en/forecasts/datasets/reanalysis-datasets/era5; GPCP at http://gpcp.umd.edu/. Any other data are available from the corresponding author upon request.

APPENDIX

Bjerknes–Wyrkti–Jin Stability and Periodicity Indices

According to the mixed layer heat budget equation [Eq. (5)], the ENSO SSTA tendency equation for the Niño-3 region can be written as follows:

$$\frac{\partial T_E}{\partial t} = \underbrace{-\left[\frac{\partial \overline{u}T'}{\partial x} + \frac{\partial \overline{v}T'}{\partial y}\right]}_{\text{DD}} + \underbrace{\frac{[\overline{w}_H T'_H]}{H}}_{\text{TH}} - \underbrace{\left[u'\frac{\partial \overline{T}}{\partial x}\right]}_{\text{ZA}} - \underbrace{\left[v'\frac{\partial \overline{T}}{\partial y}\right]}_{\text{MA}} - \underbrace{\left[w'\frac{\partial \overline{T}}{\partial z}\right]}_{\text{VA}} - \underbrace{\left[u'\frac{\partial T'}{\partial x} + v'\frac{\partial T'}{\partial y} + w'\frac{\partial T'}{\partial z}\right]}_{\text{NDH}} + \underbrace{\frac{[Q']}{\rho_0 C_p H}}_{\text{TD}} + \underbrace{[Q_{\text{SG}}]}_{\text{SG}}, \tag{A1}$$

where the square brackets represent the volume average within the mixed layer in the Niño-3 region, and w_H and T_H are the vertical ocean current and ocean temperature at the bottom of mixed layer. The terms on the right side of Eq. (A1) are dynamic damping by horizontal mean currents (DD), thermocline feedback (TH), zonal advective feedback (ZA), meridional advective feedback (MA), vertical advective feedback (VA), nonlinear advective dynamic heat (NDH), thermal damping (TD), and subgrid-scale contributions (SG). According to S. Zhao and F.-F. Jin (2021, unpublished manuscript), the quasi-balance approximation linear relationships in the analysis of Bjerknes–Wyrkti–Jin (BWJ) stability and periodicity indices can be derived from the Cane–Zebiak framework (Cane and Zebiak 1985) and be expressed as

$$T_H = e_1 T_E + e_2 T_{\text{sub}}, \tag{A2a}$$

$$T_{\text{sub}} = a_h h_e, \tag{A2b}$$

$$h_e - h_w = \beta_T T_E, \tag{A2c}$$

$$u = \beta_{uT} T_E + \beta_{uh} h_w, \tag{A2d}$$

where T_{sub} is the subsurface temperature at 75-m depth, and h_w and h_e are the thermocline depth anomalies over the western Pacific (5°S–5°N, 120°E–155°W) and eastern Pacific (5°S–5°N, 155°–80°W), respectively. Applying the quasi-balance approximation linear relationships [Eqs. (A2a)–(A2d)], the ENSO SSTA tendency equation is written as follows:

$$\frac{\partial T_E}{\partial t} = \underbrace{-\alpha_{\text{DD}} T_E}_{\text{DD}} + \underbrace{\frac{[\overline{w}_H M(\overline{w}_H)]}{H}\{(e_1 + e_2 a_h \beta_T) T_E + e_2 a_h h_w\}}_{\text{TH}} - \underbrace{\left[\frac{\partial \overline{T}}{\partial x}\right](\beta_{uT} T_E + \beta_{uh} h_w)}_{\text{ZA}} + \underbrace{(R_{\text{MA}} T_E + F_{1_{\text{MA}}} h_w)}_{\text{MA}} + \underbrace{(R_{\text{VA}} T_E + F_{1_{\text{VA}}} h_w)}_{\text{VA}} + \underbrace{(R_{\text{NDH}} T_E + F_{1\text{NDH}} h_w)}_{\text{NDH}} - \underbrace{\alpha_{\text{TD}} T_E}_{\text{TD}} + \underbrace{(R_{\text{SG}} T_E + F_{1_{\text{SG}}} h_w)}_{\text{SG}}, \tag{A3}$$

where $M(\overline{w}_H)$ is a Heaviside function, which is defined as being zero when $\overline{w}_H \le 0$ and one when $\overline{w}_H > 0$. The coefficients in Eq. (A3) can be obtained by the linear regression (S. Zhao and F.-F. Jin 2021, unpublished manuscript). According to Eqs. (1) and (A3), the SST growth rate R and phase-transition rate F_1 are expressed as

$$R = -\alpha_{\mathrm{DD}} + \frac{[\overline{w}_H M(\overline{w}_H)]}{H}(e_1 + e_2 a_h \beta_T) + \left[-\frac{\partial \overline{T}}{\partial x}\right]\beta_{uT} + R_{\mathrm{MA}} + R_{\mathrm{VA}} + R_{\mathrm{NDH}} - \alpha_{\mathrm{TD}} + R_{\mathrm{SG}}, \quad \text{(A4a)}$$

$$F_1 = e_2 a_h \frac{[\overline{w}_H M(\overline{w}_H)]}{H} + \left[-\frac{\partial \overline{T}}{\partial x}\right]\beta_{uh} + F1_{\mathrm{MA}} + F_{1_{\mathrm{VA}}} + F_{1_{\mathrm{NDH}}} + F_{1_{\mathrm{SG}}}. \quad \text{(A4b)}$$

The growth rate terms on right side of (A4a) represent DD, TH, ZA, MA, VA, NDH, TD, and SG. The phase-transition terms on the right side of (A4b) represent TH, ZA, MA, VA, NDH, and SG.

REFERENCES

Adler, R. F., and Coauthors, 2003: The version-2 Global Precipitation Climatology Project (GPCP) monthly precipitation analysis (1979–present). *J. Hydrometeor.*, **4**, 1147–1167, https://doi.org/10.1175/1525-7541(2003)004<1147:TVGPCP>2.0.CO;2.

An, S.-I., and B. Wang, 2000: Interdecadal change of the structure of the ENSO mode and its impact on the ENSO frequency. *J. Climate*, **13**, 2044–2055, https://doi.org/10.1175/1520-0442(2000)013<2044:ICOTSO>2.0.CO;2.

——, and F.-F. Jin, 2001: Collective role of thermocline and zonal advective feedbacks in the ENSO mode. *J. Climate*, **14**, 3421–3432, https://doi.org/10.1175/1520-0442(2001)014<3421:CROTAZ>2.0.CO;2.

——, Y.-G. Ham, J.-S. Kug, F.-F. Jin, and I.-S. Kang, 2005: El Niño–La Niña asymmetry in the Coupled Model Intercomparison Project simulations. *J. Climate*, **18**, 2617–2627, https://doi.org/10.1175/JCLI3433.1.

Battisti, D. S., and A. C. Hirst, 1989: Interannual variability in a tropical atmosphere–ocean model: Influence of the basic state, ocean geometry and nonlinearity. *J. Atmos. Sci.*, **46**, 1687–1712, https://doi.org/10.1175/1520-0469(1989)046<1687:IVIATA>2.0.CO;2.

Bayr, T., M. Latif, D. Dommenget, C. Wengel, J. Harlaß, and W. Park, 2018: Mean-state dependence of ENSO atmospheric feedbacks in climate models. *Climate Dyn.*, **50**, 3171–3194, https://doi.org/10.1007/s00382-017-3799-2.

——, C. Wengel, M. Latif, D. Dommenget, J. Lübbecke, and W. Park, 2019: Error compensation of ENSO atmospheric feedbacks in climate models and its influence on simulated ENSO dynamics. *Climate Dyn.*, **53**, 155–172, https://doi.org/10.1007/s00382-018-4575-7.

Behringer, D. W., and Y. Xue, 2004: Evaluation of the global ocean data assimilation system at NCEP: The Pacific Ocean. *Eighth Symp. on Integrated Observing and Assimilation Systems for Atmosphere, Oceans, and Land Surface*, Seattle, WA, Amer. Meteor. Soc., 2.3, https://ams.confex.com/ams/pdfpapers/70720.pdf.

Bellenger, H., E. Guilyardi, J. Leloup, M. Lengaigne, and J. Vialard, 2014: ENSO representation in climate models: From CMIP3 to CMIP5. *Climate Dyn.*, **42**, 1999–2018, https://doi.org/10.1007/s00382-013-1783-z.

Caldwell, P. M., and Coauthors, 2019: The DOE E3SM coupled model version 1: Description and results at high resolution. *J. Adv. Model. Earth Syst.*, **11**, 4095–4146, https://doi.org/10.1029/2019MS001870.

Cane, M. A., and S. E. Zebiak, 1985: A theory for El Niño and the Southern Oscillation. *Science*, **228**, 1085–1087, https://doi.org/10.1126/science.228.4703.1085.

Capotondi, A., A. Wittenberg, and S. Masina, 2006: Spatial and temporal structure of tropical Pacific interannual variability in 20th century coupled simulations. *Ocean Modell.*, **15**, 274–298, https://doi.org/10.1016/j.ocemod.2006.02.004.

——, Y.-G. Ham, A. Wittenberg, and J.-S. Kug, 2015: Climate model biases and El Niño Southern Oscillation (ENSO) simulation. *U.S. CLIVAR Variations*, No. 13, U.S. International CLIVAR Project Office, Southampton, United Kingdom, 21–25.

——, A. T. Wittenberg, J.-S. Kug, K. Takahashi, and M. McPhaden, 2020a: ENSO diversity. *El Niño Southern Oscillation in a Changing Climate*, Amer. Geophys. Union, 65–86, https://doi.org/10.1002/9781119548164.ch4.

——, C. Deser, A.S. Phillips, Y. Okumura, and S. M. Larson, 2020b: ENSO and Pacific decadal variability in the Community Earth System Model version 2. *J. Adv. Model. Earth Syst.*, **12**, e2019MS002022, https://doi.org/10.1029/2019MS002022.

Carton, J. A., G. A. Chepurin, and L. Chen, 2018: SODA3: A new ocean climate reanalysis. *J. Climate*, **31**, 6967–6983, https://doi.org/10.1175/JCLI-D-18-0149.1.

Chen, C., M. A. Cane, A. T. Wittenberg, and D. Chen, 2017: ENSO in the CMIP5 simulations: Life cycles, diversity, and responses to climate change. *J. Climate*, **30**, 775–801, https://doi.org/10.1175/JCLI-D-15-0901.1.

Chen, H.-C., and F.-F. Jin, 2021: Simulations of ENSO phase-locking in CMIP5 and CMIP6. *J. Climate*, **34**, 5135–5149, https://doi.org/10.1175/JCLI-D-20-0874.1.

Choi, K.-Y., G. A. Vecchi, and A. T. Wittenberg, 2013: ENSO transition, duration, and amplitude asymmetries: Role of the nonlinear wind stress coupling in a conceptual model. *J. Climate*, **26**, 9462–9476, https://doi.org/10.1175/JCLI-D-13-00045.1.

——, ——, and ——, 2015: Nonlinear zonal wind response to ENSO in the CMIP5 models: Roles of the zonal and meridional shift of the ITCZ/SPCZ and the simulated climatological precipitation. *J. Climate*, **28**, 8556–8573, https://doi.org/10.1175/JCLI-D-15-0211.1.

Cox, M. D., 1980: Generation and propagation of 30-day waves in a numerical model of the Pacific. *J. Phys. Oceanogr.*, **10**, 1168–1186, https://doi.org/10.1175/1520-0485(1980)010<1168:GAPODW>2.0.CO;2.

Cravatte, S., W. S. Kessler, N. Smith, and S. E. Wijffels, 2016: First report of TPOS 2020. GOOS-215, 200 pp., http://tpos2020.org/first-report/.

Danabasoglu, G., and Coauthors, 2020: The Community Earth System Model Version 2 (CESM2). *J. Adv. Model. Earth Syst.*, **12**, e2019MS001916, https://doi.org/10.1029/2019MS001916.

DiNezio, P. N., B. P. Kirtman, A. C. Clement, S. Lee, G. A. Vecchi, and A. Wittenberg, 2012: Mean climate controls on the simulated response of ENSO to increasing greenhouse gases. *J. Climate*, **25**, 7399–7420, https://doi.org/10.1175/JCLI-D-11-00494.1.

Ding, H., M. Newman, M. A. Alexander, and A. T. Wittenberg, 2020: Relating CMIP5 model biases to seasonal forecast skill in the tropical Pacific. *Geophys. Res. Lett.*, **47**, e2019GL086765, https://doi.org/10.1029/2019GL086765.

Eisenman, I., L. Yu, and E. Tziperman, 2005: Westerly wind bursts: ENSO's tail rather than the dog? *J. Climate*, **18**, 5224–5238, https://doi.org/10.1175/JCLI3588.1.

Eyring, V., S. Bony, G. A. Meehl, C. A. Senior, B. Stevens, R. J. Stouffer, and K. E. Taylor, 2016: Overview of the Coupled Model Intercomparison Project Phase 6 (CMIP6) experimental design and organization. *Geosci. Model Dev.*, **9**, 1937–1958, https://doi.org/10.5194/gmd-9-1937-2016.

Gebbie, G., I. Eisenman, A. Wittenberg, and E. Tziperman, 2007: Modulation of westerly wind bursts by sea surface temperature: A semistochastic feedback for ENSO. *J. Atmos. Sci.*, **64**, 3281–3295, https://doi.org/10.1175/JAS4029.1.

Giese, B. S., and S. Ray, 2011: El Niño variability in Simple Ocean Data Assimilation (SODA), 1871–2008. *J. Geophys. Res.*, **116**, C02024, https://doi.org/10.1029/2010JC006695.

Golaz, J. C., and Coauthors, 2019: The DOE E3SM Coupled Model version 1: Overview and evaluation at standard resolution. *J. Adv. Model. Earth Syst.*, **11**, 2089–2129, https://doi.org/10.1029/2018MS001603.

Graham, F. S., A. T. Wittenberg, J. N. Brown, S. J. Marsland, and N. J. Holbrook, 2017: Understanding the double peaked El Niño in coupled GCMs. *Climate Dyn.*, **48**, 2045–2063, https://doi.org/10.1007/s00382-016-3189-1.

Griffies, S. M., and Coatuhors, 2015: Impacts on ocean heat from transient mesoscale eddies in a hierarchy of climate models. *J. Climate*, **28**, 952–977, https://doi.org/10.1175/JCLI-D-14-00353.1.

Guilyardi, E., A. Wittenberg, A. Fedorov, M. Collins, C. Wang, A. Capotondi, G. J. van Oldenborgh, and T. Stockdale, 2009: Understanding El Niño in ocean–atmosphere general circulation models: Progress and challenges. *Bull. Amer. Meteor. Soc.*, **90**, 325–340, https://doi.org/10.1175/2008BAMS2387.1.

——, H. Bellenger, M. Collins, S. Ferrett, W. Cai, and A. Wittenberg, 2012: A first look at ENSO in CMIP5. *CLIVAR Exchanges*, No. 58, International CLIVAR Project Office, Southampton, United Kingdom, 29–32.

——, A. Capotondi, M. Lengaigne, S. Thual, and A. T. Wittenberg, 2020: ENSO modeling: History, progress, and challenges. *El Niño Southern Oscillation in a Changing Climate*, Amer. Geophys. Union, 201–226, https://doi.org/10.1002/9781119548164.ch9.

Ham, Y.-G., and J.-S. Kug, 2012: How well do current climate models simulate two types of El Niño? *Climate Dyn.*, **39**, 383–398, https://doi.org/10.1007/s00382-011-1157-3.

——, and ——, 2015: Improvement of ENSO simulation based on intermodel diversity. *J. Climate*, **28**, 998–1015, https://doi.org/10.1175/JCLI-D-14-00376.1.

Hansen, D., and C. A. Paul, 1984: Genesis and effects of long waves in the equatorial Pacific. *J. Geophys. Res.*, **89**, 10431, https://doi.org/10.1029/JC089iC06p10431.

Hayashi, M., and F.-F. Jin, 2017: Subsurface nonlinear dynamical heating and ENSO asymmetry. *Geophys. Res. Lett.*, **44**, 12 427–12 435, https://doi.org/10.1002/2017GL075771.

——, ——, and M. F. Stuecker, 2020: Dynamics for El Niño–La Niña asymmetry constrain equatorial-Pacific warming pattern. *Nat. Commun.*, **11**, 4230, https://doi.org/10.1038/s41467-020-17983-y.

He, J., N. C. Johnson, G. A. Vecchi, B. Kirtman, A. T. Wittenberg, and S. Sturm, 2018: Precipitation sensitivity to local variations in tropical sea surface temperature. *J. Climate*, **31**, 9225–9238, https://doi.org/10.1175/JCLI-D-18-0262.1.

Held, I. M., and Coauthors, 2019: Structure and performance of GFDL's CM4.0 climate model. *J. Adv. Model. Earth Syst.*, **11**, 3691–3727, https://doi.org/10.1029/2019MS001829.

Hendon, H. H., M. C. Wheeler, and C. Zhang, 2007: Seasonal dependence of the MJO–ENSO relationship. *J. Climate*, **20**, 531–543, https://doi.org/10.1175/JCLI4003.1.

Hersbach, H., and Coauthors, 2020: The ERA5 global reanalysis. *Quart. J. Roy. Meteor. Soc.*, **146**, 1999–2049, https://doi.org/10.1002/qj.3803.

Izumo, T., J. Vialard, M. Lengaigne, and I. Suresh, 2020: Relevance of relative sea surface temperature for tropical rainfall interannual variability. *Geophys. Res. Lett.*, **47**, e2019GL086182, https://doi.org/10.1029/2019GL086182.

Jiang, W., P. Huang, G. Huang, and J. Ying, 2021: Origins of the excessive westward extension of ENSO SST simulated in CMIP5 and CMIP6 models. *J. Climate*, **34**, 2839–2851, https://doi.org/10.1175/JCLI-D-20-0551.1.

Jin, F.-F., 1997a: An equatorial ocean recharge paradigm for ENSO. Part I: Conceptual model. *J. Atmos. Sci.*, **54**, 811–829, https://doi.org/10.1175/1520-0469(1997)054<0811:AEORPF>2.0.CO;2.

——, 1997b: An equatorial ocean recharge paradigm for ENSO. Part II: A stripped-down coupled model. *J. Atmos. Sci.*, **54**, 830–847, https://doi.org/10.1175/1520-0469(1997)054<0830:AEORPF>2.0.CO;2.

——, and J. D. Neelin, 1993: Modes of interannual tropical ocean–atmosphere interaction—A unified view. Part I: Numerical results. *J. Atmos. Sci.*, **50**, 3477–3503, https://doi.org/10.1175/1520-0469(1993)050<3477:MOITOI>2.0.CO;2.

——, S. T. Kim, and L. Bejarano, 2006: A coupled-stability index for ENSO. *Geophys. Res. Lett.*, **33**, L23708, https://doi.org/10.1029/2006GL027221.

——, H.-C. Chen, S. Zhao, M. Hayashi, C. Karamperidou, M. F. Stuecker, R. Xie, and L. Geng, 2020: Simple ENSO models. *El Niño Southern Oscillation in a Changing Climate*, Amer. Geophys. Union, 119–151, https://doi.org/10.1002/9781119548164.ch6.

Johnson, N., and S.-P. Xie, 2010: Changes in the sea surface temperature threshold for tropical convection. *Nat. Geosci.*, **3**, 842–845, https://doi.org/10.1038/ngeo1008.

Kao, H. Y., and J. Y. Yu, 2009: Contrasting eastern Pacific and central Pacific types of ENSO. *J. Climate*, **22**, 615–632, https://doi.org/10.1175/2008JCLI2309.1.

Kessler, W. S., 2001: EOF representations of the Madden–Julian oscillation and its connection with ENSO. *J. Climate*, **14**, 3055–3061, https://doi.org/10.1175/1520-0442(2001)014<3055:EROTMJ>2.0.CO;2.

——, M. J. McPhaden, and K. M. Weickmann, 1995: Forcing of intraseasonal Kelvin waves in the equatorial Pacific. *J. Geophys. Res.*, **100**, 10613, https://doi.org/10.1029/95JC00382.

——, and Coauthors, 2019: Second Report of TPOS 2020. GOOS-234, 265 pp., http://tpos2020.org/second-report/.

Kim, D., J.-S. Kug, I.-S. Kang, F.-F. Jin, and A. T. Wittenberg, 2008: Tropical Pacific impacts of convective momentum transport in the SNU coupled GCM. *Climate Dyn.*, **31**, 213–226, https://doi.org/10.1007/s00382-007-0348-4.

Kim, S. T., and F.-F. Jin, 2011: An ENSO stability analysis. Part II: Results from the twentieth and twenty-first century simulations of the CMIP3 models. *Climate Dyn.*, **36**, 1609–1627, https://doi.org/10.1007/s00382-010-0872-5.

——, W. Cai, F.-F. Jin, and J.-Y. Yu, 2014: ENSO stability in coupled climate models and its association with mean state. *Climate Dyn.*, **42**, 3313–3321, https://doi.org/10.1007/s00382-013-1833-6.

Kirtman, B. P., 1997: Oceanic Rossby wave dynamics and the ENSO period in a coupled model. *J. Climate*, **10**, 1690–1704, https://doi.org/10.1175/1520-0442(1997)010<1690:ORWDAT>2.0.CO;2.

Kleeman, R., and A. M. Moore, 1997: A theory for the limitation of ENSO predictability due to stochastic atmospheric transients. *J. Atmos. Sci.*, **54**, 753–767, https://doi.org/10.1175/1520-0469(1997)054<0753:ATFTLO>2.0.CO;2.

Kug, J.-S., K. P. Sooraj, D. Kim, I.-S. Kang, F.-F. Jin, Y. N. Takayabu, and M. Kimoto, 2009: Simulation of state-dependent high-frequency atmospheric variability associated with ENSO.

Climate Dyn., **32**, 635–648, https://doi.org/10.1007/s00382-008-0434-2.

——, Y.-G. Ham, J.-Y. Lee, and F.-F. Jin, 2012: Improved simulation of two types of El Niño in CMIP5 models. *Environ. Res. Lett.*, **7**, 034002, https://doi.org/10.1088/1748-9326/7/3/034002.

Leloup, J., M. Lengaigne, and J. P. Boulanger, 2008: Twentieth century ENSO characteristics in the IPCC database. *Climate Dyn.*, **30**, 277–291, https://doi.org/10.1007/s00382-007-0284-3.

Lengaigne, M., E. Guilyardi, J. P. Boulanger, C. Menkes, P. Delecluse, P. Inness, J. Cole, and J. Slingo, 2004: Triggering of El Niño by westerly wind events in a coupled general circulation model. *Climate Dyn.*, **23**, 601–620, https://doi.org/10.1007/s00382-004-0457-2.

Lloyd, J., E. Guilyardi, H. Weller, and J. Slingo, 2009: The role of atmosphere feedbacks during ENSO in the CMIP3 models. *Atmos. Sci. Lett.*, **10**, 170–176, https://doi.org/10.1002/asl.227.

——, ——, ——, and ——, 2012: The role of atmosphere feedbacks during ENSO in the CMIP3 models. Part III: The shortwave flux feedback. *J. Climate*, **25**, 4275–4293, https://doi.org/10.1175/JCLI-D-11-00178.1.

Lu, B., F. F. Jin, and H. L. Ren, 2018: A coupled dynamic index for ENSO periodicity. *J. Climate*, **31**, 2361–2376, https://doi.org/10.1175/JCLI-D-17-0466.1.

McPhaden, M. J., 2004: Evolution of the 2002/03 El Niño. *Bull. Amer. Meteor. Soc.*, **85**, 677–696, https://doi.org/10.1175/BAMS-85-5-677.

Moore, A. M., and R. Kleeman, 1999: Stochastic forcing of ENSO by the intraseasonal oscillation. *J. Climate*, **12**, 1199–1220, https://doi.org/10.1175/1520-0442(1999)012<1199:SFOEBT>2.0.CO;2.

Neelin, J. D., M. Latif, and F.-F. Jin, 1994: Dynamics of coupled ocean–atmosphere models: The tropical problem. *Annu. Rev. Fluid Mech.*, **26**, 617–659, https://doi.org/10.1146/annurev.fl.26.010194.003153.

——, D. S. Battisti, A. C. Hirst, F.-F. Jin, Y. Wakata, T. Yamagata, and S. E. Zebiak, 1998: ENSO theory. *J. Geophys. Res. Oceans*, **103**, 14 261–14 290, https://doi.org/10.1029/97JC03424.

Perigaud, C. M., and C. Cassou, 2000: Importance of oceanic decadal trends and westerly wind bursts for forecasting El Niño. *Geophys. Res. Lett.*, **27**, 389–392, https://doi.org/10.1029/1999GL010781.

Philander, S. G. H., 1978: Instabilities of zonal equatorial currents, 2. *J. Geophys. Res.*, **83**, 3679, https://doi.org/10.1029/JC083iC07p03679.

——, 1990: *El Niño, La Niña, and the Southern Oscillation*. International Geophysics Series, Vol. 46, Academic Press, 293 pp.

Planton, Y. Y., and Coauthors, 2021: Evaluating climate models with the CLIVAR 2020 ENSO metrics package. *Bull. Amer. Meteor. Soc.*, **102**, E193–E217, https://doi.org/10.1175/BAMS-D-19-0337.1.

Rasch, P. J., and Coauthors, 2019: An overview of the atmospheric component of the Energy Exascale Earth System Model. *J. Adv. Model. Earth Syst.*, **11**, 2377–2411, https://doi.org/10.1029/2019MS001629.

Ray, S., A. T. Wittenberg, S. M. Griffies, and F. Zeng, 2018: Understanding the equatorial Pacific cold tongue time-mean heat budget. Part II: Evaluation of the GFDL-FLOR coupled GCM. *J. Climate*, **31**, 9987–10 011, https://doi.org/10.1175/JCLI-D-18-0153.1.

Siongco, A. C., H. Ma, S. A. Klein, S. Xie, A. R. Karspeck, K. Raeder, and J. L. Anderson, 2020: A hindcast approach to diagnosing the equatorial Pacific cold tongue SST bias in CESM1. *J. Climate*, **33**, 1437–1453, https://doi.org/10.1175/JCLI-D-19-0513.1.

Sooraj, K. P., D. Kim, J.-S. Kug, S.-W. Yeh, F.-F. Jin, and I.-S. Kang, 2009: Effects of the low-frequency zonal wind variation on the high frequency atmospheric variability over the tropics. *Climate Dyn.*, **33**, 495–507, https://doi.org/10.1007/s00382-008-0483-6.

Stevenson, S., A. T. Wittenberg, J. Fasullo, S. Coats, and B. Otto-Bliesner, 2021: Understanding diverse model projections of future extreme El Niño. *J. Climate*, **34**, 449–464, https://doi.org/10.1175/JCLI-D-19-0969.1.

Suarez, M. J., and P. S. Schopf, 1988: A delayed action oscillator for ENSO. *J. Atmos. Sci.*, **45**, 3283–3287, https://doi.org/10.1175/1520-0469(1988)045<3283:ADAOFE>2.0.CO;2.

Sun, Y., F. Wang, and D. Z. Sun, 2016: Weak ENSO asymmetry due to weak nonlinear air–sea interaction in CMIP5 climate models. *Adv. Atmos. Sci.*, **33**, 352–364, https://doi.org/10.1007/s00376-015-5018-6.

Timmermann, A., and Coauthors, 2018: El Niño–Southern Oscillation complexity. *Nature*, **559**, 535–545, https://doi.org/10.1038/s41586-018-0252-6.

Vijayeta, A., and D. Dommenget, 2018: An evaluation of ENSO dynamics in CMIP simulations in the framework of the recharge oscillator model. *Climate Dyn.*, **51**, 1753–1771, https://doi.org/10.1007/s00382-017-3981-6.

Wang, C., and J. Picaut, 2004: Understanding ENSO physics—A review. *Earth's Climate: The Ocean–Atmosphere Interaction*, *Geophys. Monogr.*, Vol. 147, Amer. Geophys. Union, 21–48.

Wilson, D., and A. Leetmaa, 1988: Acoustic Doppler current profiling in the equatorial Pacific in 1984. *J. Geophys. Res.*, **93**, 13947, https://doi.org/10.1029/JC093iC11p13947.

Wittenberg, A. T., A. Rosati, N. C. Lau, and J. J. Ploshay, 2006: GFDL's CM2 global coupled climate models. Part III: Tropical Pacific climate and ENSO. *J. Climate*, **19**, 698–722, https://doi.org/10.1175/JCLI3631.1.

——, and Coauthors, 2018: Improved simulations of tropical Pacific annual-mean climate in the GFDL FLOR and HiFLOR coupled GCMs. *J. Adv. Model. Earth Syst.*, **10**, 3176–3220, https://doi.org/10.1029/2018MS001372.

Xie, S., and Coauthors, 2018: Understanding cloud and convective characteristics in version 1 of the E3SM atmosphere model. *J. Adv. Model. Earth Syst.*, **10**, 2618–2644, https://doi.org/10.1029/2018MS001350.

Xue, A., F.-F. Jin, W. Zhang, J. Boucharel, S. Zhao, and X. Yuan, 2020: Delineating the seasonally modulated nonlinear feedback onto ENSO from tropical instability waves. *Geophys. Res. Lett.*, **47**, e2019GL085863, https://doi.org/10.1029/2019GL085863.

Yu, J.-Y., and S. T. Kim, 2010: Relationships between extratropical sea level pressure variations and the central Pacific and eastern Pacific types of ENSO. *J. Climate*, **24**, 708–720, https://doi.org/10.1175/2010JCLI3688.1.

Yu, L., R. A. Weller, and W. T. Liu, 2003: Case analysis of a role of ENSO in regulating the generation of westerly wind bursts in the western equatorial Pacific. *J. Geophys. Res.*, **108**, 3128, https://doi.org/10.1029/2002JC001498.

Yu, Z. J., J. P. McCreary, and J. A. Proehl, 1995: Meridional asymmetry and energetics of tropical instability waves. *J. Phys. Oceanogr.*, **25**, 2997–3007, https://doi.org/10.1175/1520-0485(1995)025<2997:MAAEOT>2.0.CO;2.

Zavala-Garay, J., C. Zhang, A. M. Moore, A. T. Wittenberg, M. J. Harrison, A. Rosati, J. Vialard, and R. Kleeman, 2008: Sensitivity of hybrid ENSO models to unresolved atmospheric variability. *J. Climate*, **21**, 3704–3721, https://doi.org/10.1175/2007JCLI1188.1.

Zhang, C., and J. Gottschalck, 2002: SST anomalies of ENSO and the Madden–Julian oscillation in the equatorial Pacific. *J. Climate*, **15**, 2429–2445, https://doi.org/10.1175/1520-0442(2002)015<2429:SAOEAT>2.0.CO;2.

Zhang, T., and D. Z. Sun, 2014: ENSO asymmetry in CMIP5 models. *J. Climate*, **27**, 4070–4093, https://doi.org/10.1175/JCLI-D-13-00454.1.

Zuo, H., M. A. Balmaseda, S. Tietsche, K. Mogensen, and M. Mayer, 2019: The ECMWF operational ensemble reanalysis–analysis system for ocean and sea ice: A description of the system and assessment. *Ocean Sci.*, **15**, 779–808, https://doi.org/10.5194/os-15-779-2019.